Raman imaging in corrosion science: High-temperature oxidation of the zirconium alloys used in the nuclear industry as an example

Michel Mermoux, Christian Duriez

Raman Imaging in Corrosion Science: High Temperature Oxidation of the Zirconium Alloys Used in the Nuclear Industry as an Example

Michel Mermoux[1], Christian Duriez[2]

[1] Univ. Grenoble Alpes, Univ. Savoie Mont Blanc, CNRS, Grenoble INP, LEPMI, 38000, Grenoble, France

[2] Institut de Radioprotection et de Sûreté Nucléaire, PSN-RES, Cadarache BP 3, 13 115 St Paul-Lez-Durance Cedex, France

Corresponding Author: michel.mermoux@lepmi.grenoble-inp.fr

Abstract

Successive technological improvements have made Raman imaging systems very efficient. Raman imaging applications now cover a wide range of scientific fields, including high temperature materials corrosion, also known as dry corrosion. The analysis of the phenomena occurring during corrosion requires knowledge in metallurgy, thermodynamics, chemical kinetics, solid state chemistry and physics. Part of this information (crystallographic phases, stress state, oxygen transport, …) can be obtained, at least qualitatively, from the analysis of Raman images of the oxidation layer. Throughout this paper, we consider as a prototypal example the oxidation of a particular zirconium alloy, Zircaloy-4, used in the nuclear industry as cladding materials in light-water reactors. Through some examples, the aim of the present paper is to describe what kind of information this method can bring, to review its merits and weaknesses. The analysis protocols methods described herein are not exhaustive, but most probably represent a simple way to read and understand the Raman images. These few examples show that rather subtle details that concern phase distribution, strain and oxygen transport can effectively be captured by this method. Most probably, Raman imaging may be applied to other alloys or systems as well.

Key Words: Raman Imaging, Zircaloy-4 oxidation, ^{18}O labelling, residual stress

1. Introduction

In 1975, Delhaye and Dhamelincourt (LASIR, Lille) introduced the first “Raman microscope” known as the MOLE microprobe, and described different approaches for Raman imaging.[1] Since then, these imaging methodologies were classified as either “global” or “point” imaging techniques.[2,3] In the “global”, wide-field, approach all spatial points of the Raman image in a specific wavenumber range are determined simultaneously from a single measurement of a globally illuminated sample. At present, this first method is only rarely implemented. By contrast, “point” imaging requires a high number of spectra to be recorded, to get the entire so-called “spectral hypercube” data set. Then,

Raman images can be reconstructed from the information available in all the individual spectra. This second approach, much slower but which gives a much more complete information, is the one now used and implemented by the main manufacturers. Since these pioneering works, tremendous progress was made in the instrument designs to circumvent the main limitation of this technique, namely its rather low sensitivity. Instrumental developments made during the last two decades led to integrated and compact instruments with “high”, submicron spatial resolution thanks to different confocal designs, greater versatility with more lasers wavelengths available and faster measurement thanks to more efficient optical designs and more and more sensitive detectors. These successive technological improvements have made Raman imaging systems commercially available, easy to use, and ready for practical, everyday-life analysis needs. Nowadays, using state of art contemporary spectrometers, the acquisition time of an individual spectrum may be at the second time scale, or even less. This means that Raman images can be acquired on rather wide dimensions, hundred square micrometers or even more, with “reasonable” acquisition times, still keeping µm spatial resolution. These datasets, which may contain several tens of thousands of spectra, can now be handled using conventional laptop computers with different analysis protocols.

From the Rayleigh criterion, Raman spectroscopic mapping or imaging microscopy allows probing materials or even complete devices at different scales, down to micrometer-to-sub-micrometer scale. The spectroscopic images, as functions various parameters (for example the intensity, peak position and width of a particular Raman line) and spatial coordinates, allow an assessment of the heterogeneity of a specimen in terms of chemical and/or physical properties. This means that Raman imaging applications cover a wide range of scientific fields, in particular in material sciences, as, for example, in the analysis of semiconductors, ceramic materials, composites, polymers, artwork, minerals…,[4] including the study of corrosion phenomena.

As demonstrated by different studies,[5] it is acknowledged that the cost of corrosion to society is significant. Moreover, these costs usually do not take into account safety or environmental consequences. Through proper corrosion management, significant cost savings can be achieved over the lifetime of an asset. Obviously, this still raises many studies worldwide. Corrosion is understood as the gradual destruction of materials (usually a metal, but not necessary) by chemical and/or electrochemical reaction with their environment. This is a process that converts a metal, an alloy or even a ceramic material into more chemically stable forms such as oxides, hydroxides, sulfides.... It is usually appropriate to distinguish between low temperature or wet/atmospheric processes from the high temperature ones. As many works have shown, in both cases, Raman spectroscopy is a convenient tool to analyze the corrosion products, for identification purposes in particular. Technically, the analysis of materials formed close to room temperature is generally much more demanding because the phases formed are generally poorly thermally stable. Consequently, very low power densities at the sample have to be used so as not to modify the nature of the corrosion products. Thus, this is probably still a situation for which Raman imaging can still be very costly in terms of analysis time, even if some solutions, a line illumination of the sample in particular, may contribute to partially solve this issue. On the other hand, this is not the case for corrosion products formed at higher temperatures, which are generally much more thermally stable, thus less sensitive to laser illumination. In most cases, characteristic spectra can be safely recorded within seconds, and the full potential of Raman imaging can be fully exploited. Here, the main issue is that samples are examined after cooling, which necessarily induce some evolutions from the sample state at the

oxidation temperature. These evolutions are to be anticipated and if possible understood by other (*in situ*) characterization techniques before sample examination at room temperature.

Focusing on high temperature corrosion, also known as dry corrosion, it appears that these are complex phenomena, involving coupled chemical, structural, metallurgical, mechanical and micro-textural (grain size, preferential orientation, open porosity, …) aspects. Understanding the corrosion mechanisms therefore *a priori* requires crystallographic and mechanical (so-called "stress" state) data, as well as data on the anionic and/or cationic transport through the corrosion layers. Obviously, this information has to be obtained *vs* time and/or corrosion layer thickness. Some of these issues can be addressed, at least qualitatively, using Raman spectroscopy. Moreover, knowing that corrosion layers formed on metal alloys are only rarely homogeneous, Raman spectroscopy and Raman imaging are obviously methods that can provide a great deal of information.

Throughout this paper, we will consider the oxidation of zirconium (Zr) alloys used in the nuclear industry as an example. Zr alloys are used worldwide for cladding materials in light-water reactors because of their low neutron absorption cross-section, high temperature strength and relatively low susceptibility to corrosion. Even if moderate in normal, in-service conditions, the exposure of Zircaloys to a pressurized water environment at about 350 °C, leads to oxidation, which may have some implications from efficiency and safety points of view, in particular for high burn-ups or extended service life.[6,7] Moreover, especially since the Fukushima–Daiichi accident, cladding degradation at higher temperatures, in conditions representative of hypothetical accidental scenarios in nuclear plants, is also an important concern. Scenarios related to loss of coolant accident (LOCA) in the reactor core, where the cladding material is oxidized at high temperature in a pure steam environment have been the subject of numerous investigations since many years.[8] In addition, even if of low probability, other high temperature scenarios such as spent fuel storage pool loss of coolant or loss of cooling accidents, or even assembly handling accidents, are to be considered. For such scenarios, the fuel rods may be exposed to a gaseous environments containing air and steam, thus nitrogen in particular.[9-12] For some of these accidental scenarios, it is worth reminding that the cladding material is the only barrier against fission product release in the atmosphere.

Since the 80's, Raman microscopy spectroscopy has been used as a characterization technique of such zirconia corrosion layers, both for *in-situ* or post-exposure, cross-section analysis, see for example Refs [13-18] listed chronologically, just to name a few. Here, it is perhaps not insignificant to note that one of the first studies used the MOLE microprobe to characterize zirconia debris originating from oxidized fuel-rod cladding from the Three Mile Island unit 2 accident.[13] Literature also shows that D.A. Long, for whom this special edition is intended, made an interesting contribution to this issue, suggesting a remote Raman microscopic facility allowing analysis in standard lead-shielded areas used in the nuclear industry for handling of radioactive material.[15] Such facilities are now implemented in a few laboratories, allowing daily the analysis of radio-active materials.

To our knowledge, Raman imaging has been used more scarcely to understand Zircaloy corrosion, even if its use tends to emerge recently.[19-22] For different reasons, Zr corrosion layers are well suited to this type of analysis, providing their thicknesses are higher than a few µm. As a matter of fact, the

analysis of cross-sectional metallographic preparations gives much more information than more usual analysis from the sample surface. Here, one must keep in mind that any given oxide layer examined represents a snapshot of the corrosion process. To follow the oxidation kinetics and to gain insight on the corrosion mechanisms, it is necessary to examine several snapshots of the same oxide. This is beyond the scope of this work, throughout this paper, kinetics of Zircaloys oxidation will not be described and discussed in detail. For this, we refer the reader to previous studies,[6-12] and references herein. Only a brief review will be given to introduce the technological context and the purpose of the measurements.

The aim of the present paper is rather to highlight some possible applications of Raman imaging techniques to corroding systems, to describe what kind of information this method can bring, and to review its present merits and weaknesses. For such a purpose, we will focus on one particular Zr alloy, namely the tin-based Zircaloy 4 (Zy-4). We will successively describe how to get information on the different phases present and their location, on the so-called residual stresses, and on the oxygen transport in the oxide layers. At each step, we describe the purpose of the measurements, give a short theoretical background, and finally some concrete examples.

The methods described herein are not exhaustive, but most probably represent a simple way to read and understand the Raman images.

2. The corrosion of zirconium alloys: technological context and brief description of the Low and High temperature corrosion phenomena

From a technological viewpoint, Zr alloys are used worldwide in water cooled nuclear power plants, either pressurized water reactors (PWRs) or boiling water reactors (BWRs). The nuclear fuel used in these reactors is in the form of fuel rods, which consist of long tubes (approximately 4 m long, with approximately 1 cm diameter and 0.6 mm wall thickness) made out of Zr alloys, which contain the fuel in the form of uranium dioxide or MOX (Mixed oxide fuel) pellets. These tubes, termed the nuclear fuel cladding, constitute the only barrier against the release of fission products into the water primary cooling circuit. Because of this function, it is crucial to nuclear safety to ensure cladding integrity during service. Various degradation processes may challenge the integrity of the cladding tube, whether under normal operating conditions, or in accidental conditions at much higher temperatures.

A commonly accepted macroscopic description of the corrosion kinetics of zirconium-based alloys divides this process into two different regimes: an initial pre-transition period, for which the oxide layer is mostly protective, and a post-transition one exhibiting faster kinetics. The onset of the accelerated corrosion regime is called the “kinetic transition” and is characterized by either the exposure time or by the oxide thickness at which the change in kinetics occurs. This kinetic transition obviously depends on the oxidation conditions, *i.e*. on the temperature and oxidizing atmosphere. However, in reviewing the corrosion data with more scrutiny, it is observed that this simple description of the kinetics is only a first approximation. More in detail, for temperature conditions close to those used in power plants, *i.e.* about 350°C (in the following, we will refer as “low” temperature (LT) conditions), Zircaloys are known to oxidize in a periodic manner. This periodic phenomenon is found whatever the oxidation conditions: pressurized water, water vapor or air. The

initially rapid oxide growth rate slows down to a low steady rate during the first oxidation cycle. After some time, the "kinetic transition" is reached, whereupon the oxide growth rate once again becomes rapid, then decelerates until the next transition.[6,7] After several of these cycles, the alloys oxidize continuously at a more rapid linear rate.[6] This periodic nature of the kinetics was mostly analyzed using simulating pressure and temperature conditions, *i.e*. in the absence of irradiation.

Zr alloys are unique in that very small changes in alloy composition (addition of about 1-2% of Sn or Nb in particular) or microstructure can cause significant differences, both in corrosion rate (pre-transition kinetics) and in oxide stability (transition or breakaway kinetics). Modern zirconium alloys such as ZIRLO™ and $M5_{Framatome}$, that both contain Nb, show improved performances against corrosion compared to previous generation alloys such as Zy-4, which is Sn-based. However, the underlying reasons for this improved performance are still poorly understood.

Most high temperature (HT), loss-of-coolant or loss-of-cooling scenarios in the reactor core usually consider oxidation by steam only. However, there are some scenarios for which air may have access to the core. Moreover, similar scenarios that include air ingress are expected for spent fuel pools accidents. At high temperature, *i.e.* above about 700°C, nitrogen has been observed to induce a strong acceleration on the Zircaloys oxidation reaction.[9-12] After the protective, pre-transition regime, a strong increase of the oxidation rate is observed. This strong acceleration is thought to be the result of a complex reaction sequence, involving nitrogen accumulation close to the metal/oxide (M/O) interface where the oxygen chemical potential is expected to be low, its reaction with the oxygen-loaded metal to form zirconium nitride ZrN particles, and their subsequent oxidation as the oxidation front progresses inward. This particular reaction sequence induces the formation of a strongly porous, non-protective oxide.[9-12] This process was evidenced in air, in air-steam mixtures, and for steam-nitrogen atmospheres as well.[10,23] Only a very limited amount of nitrogen may initiate this particular process, as it was clearly evidenced varying the nitrogen content in oxygen/nitrogen and in steam/nitrogen mixtures.[9,10]

To illustrate the effects of corrosion on Zircaloys, some typical macrographs of the samples before after some characteristic oxidation tests are shown in Fig. 1. These tests were performed starting from Zy-4, which was intensively used in French PWRs. Macroscopically, Fig. 1.b shows the appearance of the cladding material after a LT oxidation test, intended to be representative of that observed in normal in-pile operating conditions. Here, the oxide layer was obtained after an exposure at 425°C under an oxygen-steam mixture during 250 days. Its thickness is close to 30 µm. The oxidation phenomenon is therefore rather slow, and does not strongly affect the integrity of the tube. Fig. 1.c shows the aspect of the same bare material exposed in an air atmosphere for about 2 hours at 800°C. At a first glance, the stronger degradation of the samples oxidized at higher temperatures is impressive: a much more severe degradation is clearly observed. The cladding is strongly distorted, and the outer surface of the oxide layer presents a dense network of cracks. The different colors of the outer part of the sample indicate different regions with different characteristics. From this figure, safety concerns are obvious. More in details, examining cross-sections, some of the typical features of low temperature Zr alloys corrosion are observed, see Fig. 1.d, in particular the known stratified microstructure which is identified by a network of cracks parallel to the metal/oxide (M/O) interface. There is a one-to-one correspondence between the stratified aspect of the oxide layers and the periodic oxidation kinetics. This stratified aspect was also

observed on samples extracted from power plants as well. Some cracks perpendicular to the strata are also observed. In the high temperature range, the aspect of the oxide layer looks quite different, see Fig. 1.e. One can clearly distinguish different regions in the oxide layers. First, pre- and post-transition regions are simply recognized from their respective thicknesses. In both regions, the most external layer is the dense columnar oxide grown during the protective regime. In the post-transition area, underneath this layer, a porous oxide is first observed. Then, close to the M/O interface, zirconium nitride particles (ZrN) are detected as yellowish nodules in the optical images. In this high temperature range, similar regions have been observed when a tube first oxidized at low temperature is then brought to high temperature in different atmospheres, air or air – steam atmospheres. In this case, the time to the macroscopic kinetic transition is just delayed by a few hours, depending on the pre-oxide thickness and growth conditions. The micro-structure and micro-texture of both types of oxide layers is further described in Figs. S1 and S2 (Supporting Information). In particular, one notes the presence of columnar grains elongated in the growth direction, and the rather low grain size, always much lower than ca 1 µm.

In the following, these two situations, LT and HT oxides, will be examined. These few images illustrate the complexity of the phenomenon. They also confirm the need for spatially resolved analysis techniques, whether for the determination of the various phases that may be expected in the corrosion layers, or for analyzing the thermo-mechanical aspects, which are thought to contribute, at least partially, to the loss of protectiveness of the corrosion layers.

Excluding transmission electron microscopy (TEM), two techniques can, at least qualitatively, provide this information, namely synchrotron-based X-ray micro-diffraction and Raman spectroscopy. In both cases, the µm scale is relevant. Both techniques were already used in this field, that have most probably comparable and complementary merits. Nevertheless, micro-diffraction usually requires access to large facilities, which necessarily limits the number of measurements in a given time frame. In the following, whenever possible, we will also try to make the link between these two techniques. We just emphasize here that the discrimination between the different allotropic forms of zirconia, the distinction between the tetragonal and cubic forms in particular, is *a priori* easier from Raman spectroscopy, especially in the case where they are intimately mixed.

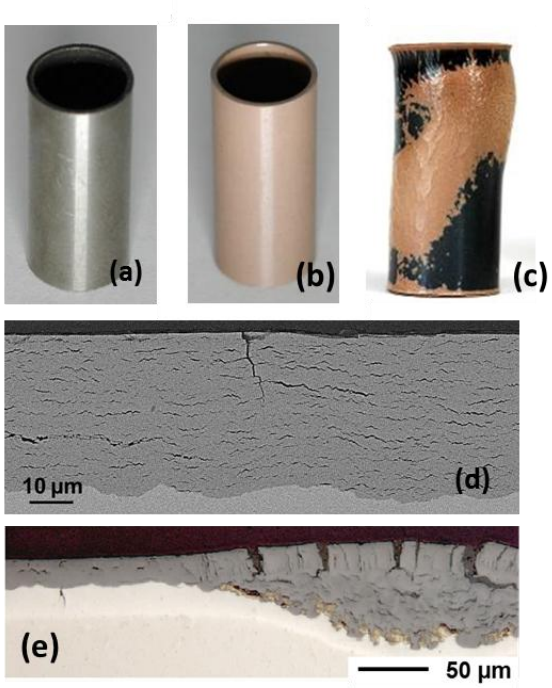

Fig. 1*: Typical features of the samples examined in this work. (a): bare Zy-4 alloy. (b): LT oxidation conditions (256 days at 425°C in 0_2-H_2O atmosphere). (c): HT oxidation conditions (2 h at 800°C, in air). (d): Cross-sectional SEM image of the LT sample. (e): Cross-sectional optical image of the HT sample.*

3. Experimental and methods

3.1. Samples.

The samples examined throughout this work have been obtained during the course of a long term experimental program launched by the "Institut de Radioprotection et de Sûreté Nucleaire" (IRSN). The rationale behind this program is to study the behavior of spent fuel pools (SFP) under loss of cooling or loss of coolant conditions. Within the framework of this project, particular attention was paid to the degradation of the fuel cladding in the event of dewatering of the assemblies. The temperature range investigated was restricted to 700–950 °C. Above about 1000 °C, the oxidation reaction in air-containing atmospheres becomes so fast that runaway of the accident looks unavoidable. A specificity of the spent fuel pool accidents scenarios is the possible presence of air in the oxidizing atmosphere around the rods when they are uncovered. Another specificity is that, because spent fuels are concerned, the presence of corrosion oxide layers formed during normal operation in reactor has also to be considered in the oxidation process, meaning that both bare alloys and pre-oxidized samples were further oxidized at high temperature. Throughout this paper, a few specific samples will be examined, with the purpose to describe the relevance of Raman imaging to their characterization and the analysis protocols that can be used according to the information sought.

Different Zy-4 alloy batches supplied by AREVA were used as received. Their composition is given elsewhere.[12] The samples were either available in the form of flat square coupons of approximate

size 10 x 10 mm, cut from 425 µm thick plates, or cut from industrial fuel cladding tubes in the form of 20 mm long specimens. LT oxidations were performed either in a horizontal resistive furnace at 425°C in a mixed O_2-steam atmosphere, or conducted in a static isothermal autoclave operating at 360°C in simulated primary water chemistry, at a pressure of about 155 MPa. High temperature oxidation experiments were systematically performed in a SETARAM SETSYS thermobalance. Different temperatures and oxidizing atmospheres were used which will be described on a case-by-case basis thereafter. For different reasons, the use of ^{18}O in the oxidizing atmosphere was also considered. In such a situation, the gas composition was continuously monitored *vs* time using mass spectrometry. A more complete description of the experimental protocols that were used may be found in Duriez et al.[12] For all samples, metallographic cross-sections were prepared from the oxidized samples. The cross-sections were polished with SiC papers, then diamond suspensions, and finally colloidal silica solutions.

Commercially available reference ZrO_2 allotropes (Tosoh, Japan), of monoclinic, Y-stabilized tetragonal and cubic structures (m-ZrO_2, t-ZrO_2 and c-ZrO_2 respectively) as well as zirconium nitride (Goodfellow, England and H.C. Starck, Germany) available in the form of powder or ceramics, were first used to get reference spectra. As we will see, m-ZrO_2 is always the predominant crystalline phase in these oxidation layers, and most of the information relative to strain and oxygen transport was obtained from the analysis of specific lines of its Raman spectrum. This is why special care has been given to the m-ZrO_2 reference sample. Indeed, small but significant line shifts (about 0.5 cm^{-1}) were observed comparing m-ZrO_2 spectra obtained for samples of different origins. Those line shifts likely reflect slight distortions of the m-ZrO_2 unit cell, possibly induced by residual strain, alloying, and perhaps even sub-stoichiometry. This is why a completely oxidized Zy-4 fragment was preferred to get a reference spectrum of (as far as possible) unstrained and stoichiometric monoclinic zirconia. This allowed alloying effects to be taken into account.

3.2. Data acquisition and pre-processing.

The data examined in this document were obtained using different spectrometers (Horiba Jobin Yvon T64000, Renishaw RM1000, Renishaw InVia). They will not be distinguished in what follows. Systematically, large numerical aperture (NA) optics have been used: 50 or 100x, with NA higher than 0.75. Because some unexpected signals were observed, different excitation wavelengths, in the 488 – 785 nm range, were used when necessary, at least to discriminate between Raman and photoluminescence (PL) origins. In all cases, the line shape of the signals in the wavenumber range of interest (50 - 800 cm^{-1}) did not depend on the excitation wavelength, which makes it possible to exclude the presence of particular PL signals. Note that such PL signals may be observed for some commercial m-ZrO_2 products, that are superimposed on the Raman spectrum when excited in the "green" wavelength range. Rather low power densities at the sample were used, a few $mW/\mu m^2$ at most, to exclude excessive sample heating.

Various tests carried out on a silicon single crystal have shown that these spectrometers can repeatedly determine the peak position of a Raman line with a precision much better than 0.1 cm^{-1}, which is required to consider the analysis of the mechanical behavior of the metal-oxide layer system.

The Raman images were systematically constructed with a measurement step of 1 µm or below, *i.e.* a point spacing close to the actual spatial resolution of the method for such fine-grained materials, for which the focused spot is generally ill-defined. In some particular cases, oversampling was necessary to stand out the information from the noise of the measurement. The probing depth was estimated in a conventional way, by performing in-depth profiles. This probing depth was a few microns at most, depending on the zirconia stoichiometry, thus on its optical properties, the absorption coefficient at the wavelength of analysis in particular.

As far as possible, the sizes of the examined areas were chosen to get representative maps for each sample. Typical acquisition times of individual spectra were in the 1 – 30 s range, depending on the instrument which was used, and on the signal/noise ratio needed. Minimal pre-processing was preferred since it may introduce some artifacts. For this reason, we did not attempt to smooth the data. Data pre-processing mainly consisted in spikes elimination and, when necessary, a so-called "base-line" subtraction. This second correction, which mainly consists in eliminating the PL signals (broad PL background from the sample itself, or arising from polishing residues) is always more or less subjective. PL backgrounds were fitted with polynomial functions mainly using the higher wavenumber range, beyond 900 cm^{-1}, far from the Raman signals of the sample, taking care not to modify the overall line shape of the Raman spectra. In most cases, data processing was achieved using the commercially available software packages Labspec 5 and Wire 4. When necessary, specific routines were written, mostly from Python software.

3.3. Data Processing

Depending on the information required, Raman results can be given as a variety of variables, see for example Idarraga et al.[19] To create the 2D spectral images, the spectra can be processed in different ways. For such a purpose, so-called "univariate" as well as "multivariate" methods can be used.

First, the integral intensity of the signal in a selected spectral range can be computed for each sample point. This is a very fast on-screen method, which allows an immediate examination of the results. Second, Raman images can also be obtained using band fitting procedures. In this case, each line of interest is first extracted from the spectral hypercube data set, and is fitted with an appropriate line shape. Thus, semi-quantitative or even quantitative information can be obtained on the presence/absence of a given crystalline phase, its crystallinity or strain state by plotting the intensity, position or the width of a specific Raman line as a function of the spatial coordinates.

However, even with a beam size of about 1 µm in diameter, the individual spectra may have complex line shapes, because they may be the result of the superposition of several components.[19,27] This circumstance can occur when the grain size is much lower than the probe size.

This will be the case throughout this paper, in part because the probed volume is much larger than the grain size, below a few 100 nm in every case, see Fig. S1 and S2 (Supporting Information). Thus, to improve the reading of the dataset, it becomes necessary to use so-called "spectral unmixing algorithms". As a rule, spectral unmixing is a procedure by which the measured spectrum at a particular image pixel is decomposed into a collection of constituent spectra, sometimes referred as

“endmembers”, and a set of corresponding fractions that indicate the proportion of each constituent spectrum present in the pixel.

Because these methods use the whole wavenumber range simultaneously, they are known as “multivariate methods”.[28-30] They allow spectral information to be completely related to samples composition. For such an analysis, the hyperspectral image cube is first unfolded into a matrix *D*, so that each collected spectrum occupies a row of the data matrix. The matrix has dimension *m x n*, where *m* is the total number of spectra from the data set and n is the number of variables, which are the wavenumbers at which the intensities are collected. The aim of each of the following methods is to decompose this matrix into submatrices *C* and *S*:

$$D = C \,.\, S^t + E \qquad (1)$$

Here, *D* is the *m* × *n* data matrix composed of *m* spectra and *n* wavenumbers, *C* is the *m* × *p* concentration or “scores" matrix with *p* the number of pure reference spectra, *S* is the *n* × *p* matrix consisting of pure spectra or loadings or endmembers corresponding to unit concentration, *E* is the *m* × *n* model residual noise matrix. *t* stands for matrix transpose.

At this stage, different multivariate image creation methods can be used. Basically, two types of methods are available, that use either “supervised” or “unsupervised” algorithms.

In the supervised approach, a library of reference spectra is used and each individual spectrum is simply expressed as a linear combination of the reference spectra. This approach is obviously the most intuitive one. It can give an estimation of component fractions, and can provide a basis for a semi-quantitative or even quantitative approach. Nevertheless, supervised algorithms assume that the library contains all the reference spectra that may be encountered during data collection. In other words, the sample has to be perfectly known. Reference spectra can be obtained from acquisitions on pure components, providing they are all known and available. They can also be extracted from the experimental data set. Moreover, each reference spectrum is assumed to be error-free. In practice, for a lot of reasons (strain, crystallographic texture, …) this is not feasible. Nevertheless, if the errors in a measured reference spectrum are small compared with the overall signal values, this approach remains a first good approximation. The mixing coefficients, *i.e.* the concentration or score matrix, are obtained from least square methods. Note that the resulting fraction estimates are based upon the data collected, and may not lead to true volume fraction calculations, due to strong differences in scattering cross-sections of the different pure phases, and/or to sampling considerations. However, they are an indication of the presence or absence of a given phase at a given location of the area analyzed. As we will see, this first approach may require looking at all the individual spectra, which is time consuming, and can be prone to errors in the case of an unknown system, or of files containing a very large number of spectra.

The purpose of the unsupervised approaches, also known as chemometric methods, is to estimate the spectra and mixing coefficients directly from measurements, without *a priori* knowledge of the sample. Allowing the potential qualification and quantification of complex systems, the role of chemometrics in the analysis of Raman spectroscopy data is becoming increasingly important for many different application areas.[28-30] Herein, two different methods, principal component analysis and multivariate curve resolution, were tested to confirm or refute the main trends obtained by a

simple visual analysis of the experimental data sets. Both methods are now available from the factories-supplied software packages.

Principal component analysis (PCA) may be used to analyze data variance.[31] The power of PCA lies in its ability to condense information from hundreds or thousands of spectra into a few orthogonal principal components or PCs (the so-called ‘‘loadings’’) and ‘‘scores’’, which provides a convenient tool for image visualization and feature extraction. Since each PC is obtained by maximizing the amount of variance it can explain, a PC does not necessarily correspond to one specific chemical or component, especially when several pure component spectra overlap seriously. Therefore, in a case where the dataset can be modelled and reconstructed with the use of *n* components, these first *n* PCs will represent the signal and later components merely exhibit noise. At present, such an analysis only takes seconds, even for large datasets, and allows to visualize the different areas of interest in a given Raman image quite immediately. Then, because each particular region contains a characteristic "true" Raman signature, this method provides a way to go back to the individual signatures that are characteristic of the different phases present in the sample, in an indirect way however.

Multivariate Curve Resolution (MCR) is the generic denomination of a group of techniques which intend the identification of the pure spectral response of the chemical constituents or species of an unresolved mixture from the sole information present in the original dataset, when no prior information is available about composition of these mixtures.[30-32] MCR-ALS is an algorithm that solves the MCR basic bilinear model using a constrained Alternating Least Squares algorithm (ALS) that fix *C* and optimize *S*, then fix *S* and optimize *C*, up to convergence. Physically meaningful constraints, such as non-negativity of concentration and spectral values are typically used during the ALS procedure to force the least-square solutions closer to true solutions. Here, the main interest is that this iterative method can be used when no reference spectra are available and one wishes to extract the different “pure spectra” that physically represent the different components of the samples from the image dataset. Generally, the method works particularly well when some of the components are present in pure form somewhere within the dataset.

Because these unmixing methods take into account all the information present in the data file, it is necessary to eliminate the spectral artifacts (spikes), and any type of fluctuating signal such as a non-uniform PL background. Again, this pre-processing can be more or less subjective, and more importantly time consuming. Data processing was mostly achieved in using the commercially available Wire 4 software packages.

4. Microstructural analysis. Phase distribution.

4.1. Expected crystalline phases and their characteristic Raman signatures

A quick overview of the available literature shows that, usually, two different zirconia phases are considered in the oxidation layers, namely monoclinic (m-ZrO_2) and tetragonal (t-ZrO_2).[16-18] We will restrict ourselves to the 350-950°C temperature range. In this temperature range, recent *in situ* examinations, using mainly X-ray diffraction, have shown that the average volume fraction of these two phases varies to some extent upon sample cooling.[33] This variation is all the more important as the oxidation temperature is high, but seems quite limited below 850°C. This means that the

evolution of phase fraction within the oxide thickness can be studied at RT, with some caution however. This is no longer the case for higher temperatures, 950°C and above, *i.e.* for temperatures close or above the monoclinic to tetragonal phase transition. The temperature at which the phase transition is expected depends, among other, on the pressure conditions and the size of the crystallites.[17,18]

Both ZrO_2 polymorphs were identified with local probes, *i.e.* micro-Raman[16-19] et and micro-X-ray diffraction.[34-37] These two phases can also be identified by more macroscopic methods. m-ZrO_2 is the thermodynamically stable phase in the growth conditions, and is always the predominant phase. Its identification is straightforward. 18 Raman-allowed modes of A_g and B_g symmetry are expected,[38] among which 15 or 16 are effectively observed. t-ZrO_2 is metastable in this temperature range, and it is thought to be stabilized by local particular conditions in the oxide, such as compressive stress, small grain size, dissolved alloying elements, sub-stoichiometry, or even a combination of these parameters. Its identification and distinction from the cubic phase from their corresponding Raman spectra is also straightforward. 6 Raman-allowed modes of A_{1g} and B_{1g} and E_g symmetry are expected and may be observed. The t-ZrO_2 content is known to vary with the alloy composition, oxidation temperature, as well as layer thickness, *i.e.* oxidation duration.[6,7,14] Moreover, spatially-resolved techniques, still X-ray micro-diffraction and micro-Raman spectroscopy also evidenced a higher fraction of the metastable t-ZrO_2 along the M/O interface, in the form of a thin submicron layer.[14,19,20,35-37] More in detail, there are thought to be two different populations of tetragonal phase.[19,39] Most often, the tetragonal phase, present in the vicinity of the M/O interface (from now on identified as it-ZrO_2) is associated to a protective behavior, transforming to monoclinic grains as soon as they reach a critical size.[6,14] The second population (from now on identified as bulk bt-ZrO_2) seems to be a remnant phase, present in small amounts throughout the oxide bulk.[19,39] In spite of the low thickness of the interfacial tetragonal layer, it-ZrO_2 could be observed without strong interference with the m-ZrO_2 signal. The overall appearance of the spectrum is very different from that which is known for tetragonal zirconia, either stabilized by addition of aliovalent elements or by size effect. In particular, the characteristic lines of bt-ZrO_2 usually observed at about 267 and 456 cm^{-1} are strongly shifted, by about +15 and -20 cm^{-1} respectively from their expected positions.[16,19,40] This is a direct indication of strong distortions from the usual tetragonal structure. This fact was underlined from the first Raman studies. Some micro-diffraction results also point in this direction, even if the low intensity and the low number of observable reflections of this particular phase does not allow to conclude with certainty about the nature of this distortion.[39] Other observable characteristic features are the low line width of the t-ZrO_2 280 cm^{-1} line as compared to that of the reference powder, and strong differences in the line intensity ratios between both t-ZrO_2 signals.

When the oxidizing mixture contains nitrogen, ZrN may be present as well. ZrN is mostly observed for oxidation temperatures higher than ca 700°C, in the form of nodules, most often close to the M/O interface. Their presence is not straightforward to understand. From pure thermodynamic arguments, ZrN formation means very low oxygen partial pressures, down to 10^{-30} atm, a condition that can be reached close to the metal, and obviously a nitrogen access. Their apparent stability only reflects a transient state frozen during the sample cooling step. During the oxide inward progression, they are known to progressively convert into oxide. ZrN nodules are sometimes observed for experiments in which nitrogen is not intentionally injected into the gas phase. This means that low nitrogen concentrations, perhaps at the trace level, can contribute, at least locally, to modify the

oxidation kinetics. Note that oxidation of Zr-based alloys is by far much faster in nitrogen-containing environments (oxygen and/or steam) than in nitrogen-free atmospheres. In most cases, ZrN can be detected optically, as golden colored nodules. ZrN exhibits a rather strong Raman spectrum with apparent maxima at about 200 and 500 cm^{-1}. Because it crystallizes in a rock-salt structure, ZrN is not expected to produce any first-order Raman signal. One expects to observe only broad spectral features due to two-phonons processes.[41] Nevertheless, due to some disorder in the ZrN lattice (N vacancies, micro-strain, other defects, …) these crystals loose in part their translational invariance, which in turn gives rise to a Raman spectrum reminiscent of a single phonon density of states. As such, this broad signal is a clear fingerprint of ZrN.

These 4 spectra therefore constitute the first spectra library which is necessary for data analysis, they are given in Fig. 2. As we will see below, these 4 spectra may not be sufficient to enable a complete description of all the different data files, those recorded for the oxidation of Zy-4 in particular.

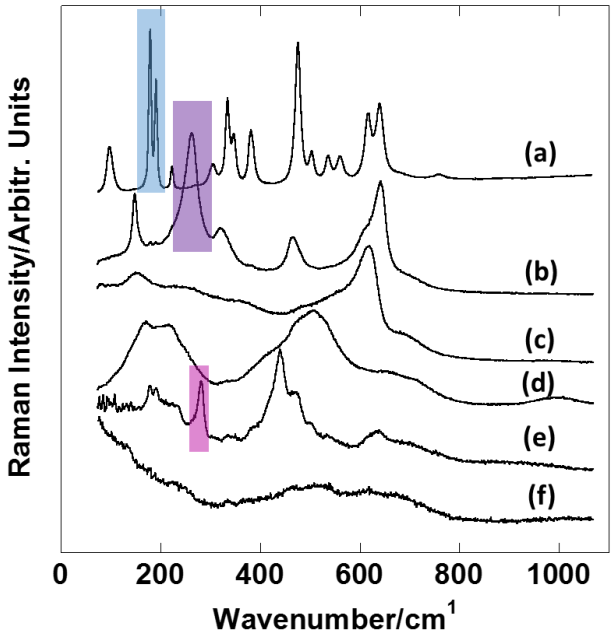

Fig. 2. *Spectra library used for the analysis of the Raman images. (a): m-ZrO_2, (b): bt-ZrO_2, (c): c-ZrO_2, (d): ZrN, (e): it-ZrO_2, (f): the broad Raman signature which seems to be specific to oxide layers formed on Zy-4. The colored areas approximatively indicate the wavenumber range which was used for the construction of the m-ZrO_2, bt-ZrO_2 and it-ZrO_2 Raman images using the integrated intensity of the signal. Note the strong difference between the line shapes of the bt- and it-ZrO_2 spectra.*

4.2. HT oxidation of Zy4. Examination of the Raman signals

To illustrate the contribution of Raman imaging for the structural analysis of these oxidation layers, we consider the example of Zy-4 oxidized at HT in air, at 800°C. This example corresponds in all respects to the analysis of a sample similar to that shown in Fig. 1.c and 1.e. This is effectively the most complex situation we have encountered so far. Here, Raman imaging was used to determine the oxide structures associated with protective and non-protective behaviors. For such a purpose, it is interesting to look at samples for which the oxidation was stopped just after the onset of the kinetic transition. Thermogravimetric monitoring allows a precise determination of this kinetic

transition, which is easily detected as the first minimum of the oxidation rate *vs* time. Then, areas characteristic of pre- and post-transitory behaviors can be found in a same sample cross-section. This sample was partially examined in Idarraga et al.[19]

On first reading, HT Zy-4 oxidation layers cannot be completely understood with the phases described above. Simple line scans across the samples immediately show that at least an additional broad signal has to be considered, see Fig. 3. In fact, this broad signal can be observed for both types of oxides. Concerning LT oxide layers, it is mostly observed for film thicknesses below than ca 10 µm, or even when thicker oxide layers are subsequently annealed above 800°C under vacuum. Most often, this feature appears superimposed on the usual m-ZrO_2 spectrum. Examining in more detail the spectra, the line shape of this signal seems to evolve along the line scan, exhibiting different apparent maxima, see Fig. 3.

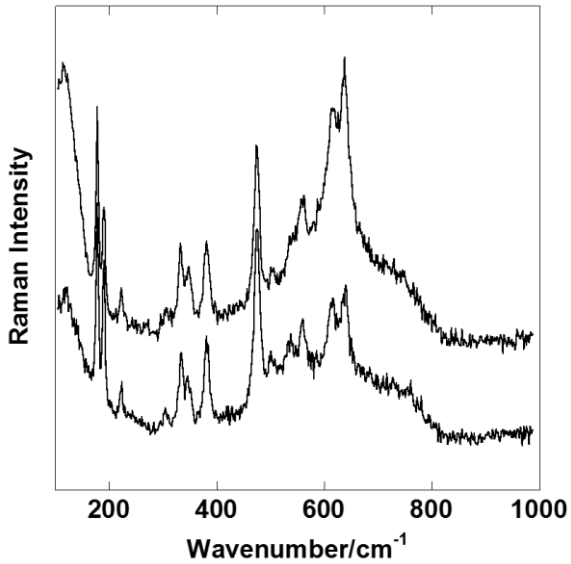

Fig. 3*: Examples of Raman spectra recorded on oxide layers grown on Zy-4. A broad contribution is clearly evidenced below the characteristic spectrum of m-ZrO2. The line shape of this broad is changing from one pixel to another. More details concerning the analysis of these signals are given in Idarraga et al.[27]*

As completely described in Idarraga et al.,[27] successive subtractions between some spectra allowed to gain more information. Such a trial and error process is time consuming, and obviously can lead to more or less questionable results. Nevertheless, it allowed to isolate two additional characteristic signatures. Quite surprisingly, the first one was the characteristic broad signature of c-ZrO_2. To our knowledge, the presence of c-ZrO_2 has never been reported before in such oxide layers. Second, further subtractions allowed to isolate a continuous background spectrum, with different apparent maxima, see Fig. 2. Again, such a feature was never mentioned in previous studies. There could be two reasons for this. First, this signal is clearly observable only by increasing the acquisition times and recording the spectra over a wide wavenumber range, well beyond the observable first-order characteristic features of all the ZrO_2 polymorphs, and well beyond the cut-off frequencies of the corresponding crystalline phases. Second, inadequate baseline corrections can contribute to partially or completely obscure this signal. So far, this signal has never been seen with such intensity for other alloys, $M5_{Framatome}$ in particular.

To ascertain the origin of all this last observed feature, a first and necessary step was to exclude the presence of some possible PL lines in this wavenumber range. Tuning the excitation wavelength from 785 to 488 nm, the absence of any significant signal variations, both in position of intensity, convincingly showed that this particular signal was due to light scattering. Moreover, it was possible to isolate this signal in particular regions of some of the examined samples, which allowed to completely confirm its line shape.

At this stage, the interpretation of this broad signal is still uncertain, but tentative assignments can be proposed.

First, this signal was clearly observed when nitrogen was injected in the gas phase, a situation for which the formation of oxynitrides cannot be excluded. For various reasons, assignment of such a signal to such compounds should probably be rejected: (i) Apart from visible ZrN nodules, the nitrogen content, as estimated with Electron Probe Micro Analysis (EPMA), is always lower than the detection threshold of the technique, *i.e.* a few%. (ii) A similar line shape was also observed in nitrogen-(virtually) free oxidation conditions. Similarly, it cannot be attributed to a $(Fe_xCr_{(1-x)})_2O_3$ phase, or to other oxidation products of the Laves $Zr(Fe,Cr)_2$ intermetallic particles, these alloying elements being in very low proportion.

As already mentioned, this signal is seen analyzing the surface of oxidation layers formed at low temperature, providing their thickness is low, below about 10 µm. For such conditions, the oxidation layer is black in color, which is a clear and known sign of oxygen sub-stoichiometry. For layers of higher thicknesses, light brown in color, the broad signal is no longer observed from analysis conducted from the sample surfaces. Moreover, when heated under vacuum, such specimens turn from light brown to a uniform black color, and the broad signal is detected once again. In such vacuum and high temperature conditions, the whole oxide thickness is expected to be chemically reduced, as a result of a strong oxygen diffusion in the metallic Zr substrate. Thus, it is first tempting to interpret this particular signal in terms of disorder or sub-stoichiometry in the O sub-lattice. Such a translational disorder introduced by vacancies may lead to a breakdown of the k≈0 selection rules. In the case of a strong disorder, the reduced Raman spectra ultimately represent the frequency distribution of the phonon density of states (VDOS). In the present case, the observed broad signal has an apparent cut-off at about 830 cm^{-1}, which matches the cut-off wavenumbers of the m-ZrO_2, t-ZrO_2, and even c-ZrO_2 polymorphs computed VDOS.[38,42-45] Moreover, upon ^{18}O isotopic substitution, the whole high wavenumber part of the spectrum is downshifted, more or less as expected for O-dominated vibration modes.[46] Such a downshift unambiguously reveals phononic contributions to the Raman spectrum, and that this broad signal involves an oxygen sub-lattice.

Finally, because it was not clearly observed for other alloys, the main alloying element, Sn in particular, was also considered. At first glance, this signal cannot be assigned to any known crystalline SnO_2 phase. Nevertheless, broad and unresolved Raman signatures may be observed in very fine sub-stoichiometric SnO_{2-x} nanoparticles.[47] Such signals are observed in a similar wavenumber range. They also display some apparent maxima that more or less match those observed in the Zy-4 oxide layers. At present, this last hypothesis cannot be completely disregarded.

In the particular case of oxide layers grown on Zy-4, these preliminary observations therefore suggest that at least 6 distinct signatures in the image files may be expected: m-ZrO_2, it-ZrO_2, bt-ZrO_2, c-ZrO_2, ZrN, and the broad "background signal". These signatures, or model spectra are given in Fig. 2. It was verified that linear combinations of these 6 distinct "signatures" or "reference" spectra allow to reconstruct all the individual spectra that are present in the preliminary 1-D scans with low residues. [27] It is worth noting that X-ray diffraction only detects and consider two or three different phases, m- and t-ZrO_2 and ZrN when present, for similar samples.[48] These 6 signatures will be used to construct the different phase distribution images.

4.3. univariate analysis

The analyzed area is identified in the optical image by the white frame, see Fig. 4. Pre-and post-transition areas are easily recognized, and golden ZrN particles are effectively seen at the M/O interface in the post-transition area. Spectra were acquired every 0.8 µm across the oxide layer. The resulting image file contains about 8160 individual spectra. The analyzed wavenumber range was extended well beyond the characteristic wavenumber range of the expected phases, to facilitate data preprocessing, the subtraction of the PL background in particular.

A first examination of the data set shows the diversity of the individual spectra that make up the image: areas with nearly no signal (metal), low (M/O interface) and high (surface) intensity signals, broad and thin lines characteristic of the different crystallographic phases, small wavenumber shifts associated to local strain variations within the layer, … Again, even with a beam size of about 1 µm diameter, it was observed that most of the individual spectra have a complex line shape, because they are the result of the superposition of several components. This was a common observation for the oxides formed on this specific alloy. An immediate consequence is that it is difficult to isolate wavenumber ranges that are characteristic of a single phase. m- and t-ZrO_2 phases can be effectively identified and discriminated with their characteristic lines peaking in the low wavenumber range, in the 175-200 and 260-280 cm^{-1} range for m-ZrO_2 and t-ZrO_2 respectively. These wavenumber ranges are highlighted in Fig. 2. Two different wavenumber ranges have been considered for the location of the t-ZrO_2 phases. The integrated intensity into these wavenumber ranges effectively allows to construct the first composition images, see Fig. 4. a. On the other hand, this procedure is no longer possible for the other phases, which means that multivariate methods are to be used to completely describe the sample.

To reconstruct these first images, the integrated intensity of particular lines that are present in the raw signals was used. Focusing on the m-ZrO_2 lines, strong intensity variations, of about a factor of 20, are observed, with the highest and lowest intensities in the porous oxide and dense regions respectively. The decrease in intensity affects all the m-ZrO_2 lines in the same way. Deviation from stoichiometry of the zirconia likely explain all these features. m-ZrO_2 sub-stoichiometry is expected from the oxidation mechanism itself, which involve oxygen vacancy migration from the M/O interface to the oxide/gas interface. Again, hypo-stoichiometric m-ZrO_2 has a black color, whereas stoichiometric m-ZrO_2 formed from Zy-4 is of light brown color, as a probable consequence of the Lave phase oxidation that leads to formation of hematite particles. The evolution of the optical properties with oxygen sub-stoichiometry suffices to explain such variations in intensity, which are due to strong variations in the absorption of the incoming beam. In the pre-transition area, m-ZrO_2

features generally exhibit rather low intensities and broad line shapes. However, the m-ZrO_2 signal intensity strongly increases near the film surface. On the other hand, the spectra recorded in the porous region show narrow and intense m-ZrO_2 lines, which is the indication of a high structural order and a high stoichiometry of this phase. In this porous part of the scale, the continuity of the film is disrupted, which contributes to slow down oxygen exchanges with the metal, likely explaining the higher oxygen stoichiometry. Thus, the m-ZrO_2 intensity image partially reflects the oxygen stoichiometry.

This first method of image reconstruction uses the raw signals. As such, it is not prone to artifacts. On the other hand, it does not allow a complete description of the sample.

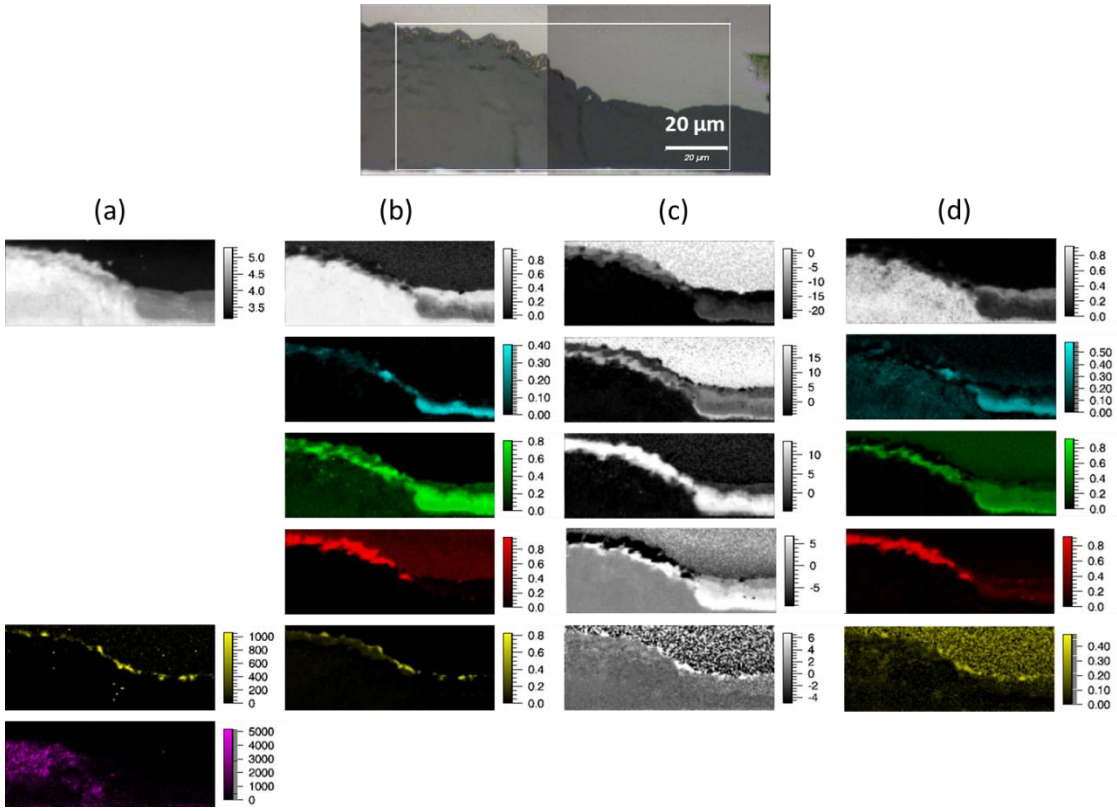

Fig. 4*: Detection of the different phases that are present in a HT Zy-4 oxide layer. Bare Zy-4 was oxidized in air, at 800°C, for 2 hours. The analyzed area (108 x 47 µm) is highlighted by the white shading. (a): univariate method. The range of signal integration is given in Fig. 2. The intensity scale is the signal integrated intensity. (b): linear combination of the model spectra given in Fig. 2. The intensity scale is the relative contribution of each component. bt-ZrO_2 is not taken into account. (c). PCA analysis of the image data file. Only the first 5 images constructed from the corresponding 5 loadings are given. The intensity scale is the score of the corresponding principal component. (d) MCR analysis of the image data file. 5 of the 7 corresponding images are given. The intensity scale is the relative contribution of each component (%). m-ZrO_2 (black & white), c-ZrO_2 (blue), the broad signal (green), ZrN (red), it-ZrO_2 (yellow) and bt-ZrO_2 (magenta) are detected and localized by the different methods.*

4.4. Multivariate analysis - Supervised approach.

To completely describe the sample, it is therefore necessary to use Multivariate methods, that take into account and analyze the whole data set simultaneously. The first method used was obviously to consider that each individual spectrum is the result of a weighted sum of the six reference spectra described above. Here, before computation, it was first necessary to subtract the PL background of each individual spectrum. Otherwise, computations never converged towards an acceptable solution. Further, the integrated intensity of all the individual spectra was normalized to unity. This normalization smoothed out the strong variations in intensity observed within the analyzed region. It was also intended to better bring out weak signals, and to allow a comparison with the PCA routine that include such a normalization step. The same data pre-processing was also applied to the model spectra. A consequence of this normalization step is that the intensity scale of the images will range between 0 (complete absence) and 1 (pure phase): the analysis will not give quantitative results. Anyway, for different reasons, a complete quantitative description would have been very difficult here.

The different images obtained from this method are given in Fig. 4.b. From the figure, it is seen that the different signals are not randomly distributed. This gives some credit to the initial hypothesis, which was based on successive subtractions between spectra as described above. ZrN and it-ZrO_2 are found in the vicinity of the M/O interface. Note also that c-ZrO_2 is detected in a specific region, with a rather low contribution to the overall signal, about 30% at maximum. The broad component is mainly seen in a particular region of the image, where the m-ZrO_2 signal intensity is weak and probably characteristic of oxygen hypo-stoichiometry. On the other hand, it was not possible to completely locate bt-ZrO_2. Its contribution was always too weak in all the individual spectra, the computation never converged to a correct solution when we tried to take it into account in the model. The best results were obtained ignoring its contribution to the data file.

This method therefore makes it possible to give a first, although incomplete, description of the sample. However, because of the base line correction and the data normalization, there may be some artifacts. Indeed, the normalization step amplifies the weak signals, and sometimes gives them too much importance in the fit. Therefore, one must consider carefully the mixing coefficients below 0.1. One can undoubtedly refine the computation by taking into account other signals (metal, eventually mounting materials), or by masking particular regions of no interest for the understanding of the oxide layers. However, this did not dramatically affect the main trends of these first computations.

4.5. Multivariate analysis– Unsupervised approaches - Testing the supervised model assumptions

As already mentioned, supervised algorithms assume that the model contains all reference spectra that may be encountered in data collection. This model has been obtained from successive subtractions between individual spectra present in the dataset. Such subtractions may be more or less subjective. It is therefore interesting, even essential, to use other algorithms to confirm or refute these initial results.

For such a purpose, the first method used was PCA. The same normalized and base line-corrected data set was used. The results of data decomposition upon the PCA procedure are partially shown in Fig. 4.c., in which only the five first PCA images are given. A more complete computation is given in Fig. 5. Ten components allowed to explain about 90% of the data variance. These components or loadings are shown in Fig. 5.a. Again, we note that the specificities of the data treatment with PCA lead to loadings which are not real spectra but "spectral-like" features, all orthogonal to each other because of the matrix diagonalization process they arise from. They can be of negative values, see for example the PC1 component.

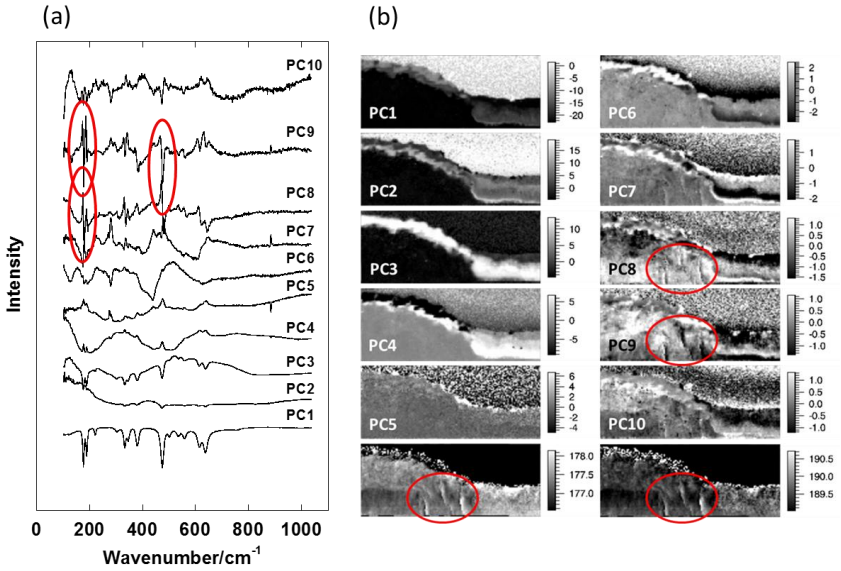

Fig. 5*: First 10 loading vectors of the spectral data shown in Fig. 3. Their corresponding variance explained are: 51.2%, 22.7%, 6.75%, 3.47%, 1.93%, 0.49%, 0.25%, 0.16%, 0.12%, 0.1%, respectively. The red circles highlight details in some of the loading vectors, a derivative- like line shape in particular, an indication of line shifts in the corresponding Raman lines. (b): Corresponding first 10 Raman images constructed with the loading vectors shown in (a). The red circles highlight some regions that are recognized both in the PCA and M2 (at about 178 cm^{-1}) and M3 (at about 190 cm^{-1}) line position images.*

The corresponding ten images are also given in Fig. 5.b. They should not be considered as true composition images. These images rather indicate where there is some variability in the Raman data: an absence of contrast in a particular region of the image is a direct indication that all the individual spectra which compose this region are similar in shape. Interestingly, a first reading of the first five images immediately shows that the different regions determined by the supervised analysis are completely reproduced, even in their finest details, see Fig. 4. In particular, regions that contain t-ZrO_2, c-ZrO_2 and ZrN are perfectly localized. For each of these regions, the different characteristic spectra detected during the visual examination of the data set, that were given in Fig. 2 and Fig. 3, are effectively recognized. However, regions for which the "bulk" t-ZrO_2 was extracted from univariate procedures are not clearly highlighted by the computation. The four last components exhibit particular signals with a first-derivative-like line shape. These signals are observed in wavenumber ranges that match some of the characteristic lines of m-ZrO_2. As such, they correspond to small individual line shifts in the image data set that translate strain variations within the sample, see for example the correspondence between the PC8, PC9, and the line position images of the

modes peaking at about 178 and 190 cm^{-1} in Fig. 5.b. These small line shifts variations will be analyzed in more details in what follows.

Second, as already mentioned, we used the MCR-ALS unmixing algorithm, which is available in the Wire 4 software package. Again, the same normalized data set was used. More complete results are given in Fig. S3 (Supporting Information). They completely confirm the trends suggested by the supervised approach. 7 "endmembers" were determined from the computation. Five of them are given in Fig. 6, the corresponding Raman images are given in Fig. 4.d. The line shape of the two last computed spectra (not shown here) are rather related to small line shifts in the m-ZrO_2 spectra. They also allow to take into account the contribution of the metal response to the data file. Five of these spectra mimic those extracted from the supervised analysis of the data set, see Fig. 6. In particular, the characteristic signatures of c-ZrO_2 and the broad signature are reproduced. More, the algorithm perfectly identifies the same areas, and gives comparable mixing coefficients, here values simply ranging from 0 to 1, in the intensity scales, see Fig. 4.d. Nevertheless, the "bulk" t-ZrO_2 contribution evidenced from univariate procedures is still ignored by the computation.

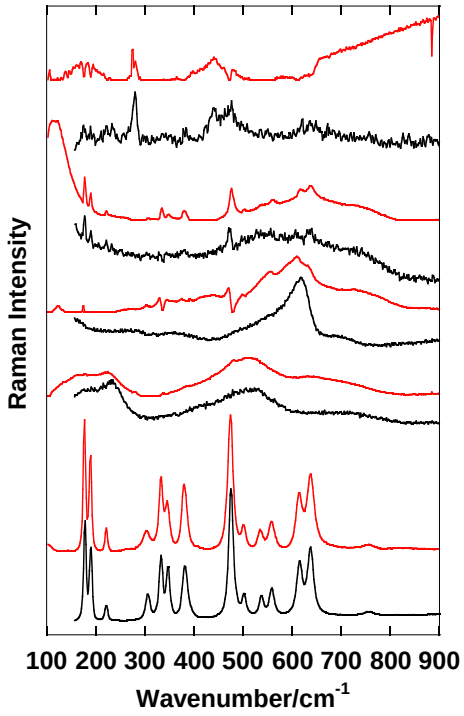

***Fig. 6**: Black traces: reference spectra used in the multivariate, supervised approach. Red traces: 5 of the 7 Raman "signatures" obtained using the MCR-ALS algorithm.*

4.6. Summary: contributions of the methods.

Looking at the different phases that may be present in those corrosion layers, this example demonstrates a first important contribution of Raman imaging: the system analyzed may be more complex than initially expected. In such a situation, X-ray diffraction fails to identify all the different phases. Moreover, X-ray diffraction does not give direct insights on the local oxygen stoichiometry. Likewise, more macroscopic Raman approaches are unable to completely describe the samples. In

most cases, they only allow to detect unambiguously the main crystallographic phase, here m-ZrO_2, and from case to case t-ZrO_2.

The analysis of data sets can be approached in several ways, thanks to supervised and unsupervised protocols. In this particular case, three different protocols converged towards a same solution, allowing for positive identification of the phases. The only exception was the bulk tetragonal oxide phase, which was not detected by both unsupervised approaches, but identified by a simple visual examination of the individual spectra as very weak spectral features. Such an identification is all the more confident as the duration of acquisition of each individual spectrum is increased. This means that a compromise between the size of the examined area, the point spacing and the overall acquisition time has to be found.

To date, only a few analyzes could be carried out on oxide layers grown on a different alloy, the $M5_{Framatome}$ one, which is now widely used in French nuclear plants. Interestingly, Raman spectroscopy and Raman imaging allows to discriminate between both alloys, in terms of crystallographic phases detected in the oxide layers. A more detailed comparison of the oxidation behavior of the 2 alloys is in progress, for both LT and HT conditions.

5. Residual stresses in the oxide layers.

5. 1. Overview.

Considering thin films, the analysis of the residual stress state is of great technological importance because as a rule, stresses can be beneficial or detrimental. From a pure mechanical viewpoint, stress can result in cracking of a film in the case of tensile stress, or buckling in the case of compressive stress. Oxidation layers can develop large residual stresses during their growth that may significantly impact their protectiveness.[49] Therefore, there is a need to understand how such stresses are related to the developing film structure and micro-structure and underlying kinetic processes, the transition from a protective regime to a non-protective one in particular. Residual stresses can be defined as stresses that remain in a material in the absence of external forces or thermal gradients. Depending on the system, these residual stresses can be observed at different length scales within the samples, and, in the absence of external forces, are balanced. They may be observed as either macro- or micro-stresses. Macro-residual stresses vary within the body of the material over a length scale much larger than the grain size, while micro-residual stresses rather operate at the grain-size level. The origins of residuals stresses in a thin film system may be roughly classified as thermal and growth stresses. Thermally generated residual stresses are the consequence of the coefficient of thermal expansion (CTE) mismatch between the different phases or constituents. Most often, the growth stresses find their origin from different chemical and/or structural processes.[49] Although the precise origins of the growth stresses are numerous and not fully understood, it is believed that they are strongly affected by the molar volumes of oxide and metal, their crystalline structures, and the growth mechanism of the oxide. When an oxide forms at a M/O interface, the volume change associated to the formation of the oxide is usually first expressed with the Pilling-Bedworth ratio (PBR). The PBR is defined as the ratio between the molar volume of the oxide and the one of the metal from which the oxide is formed. The larger the difference of PBR from 1, the larger the growth stress, either compressive or tensile. As far as Zr alloys are concerned, the

PRB is close to 1.5, meaning that strong compressive stresses are expected in the growing oxide layer. However, it is widely acknowledged that there is no direct relation between the PBR and the level of stress in the oxide layer, its direct conversion leading to completely unrealistic stress values. As mentioned above, additional stresses may arise from the polymorphic transformations of zirconia, for example the tetragonal-to-monoclinic phase transition, or ZrN oxidation to m-ZrO_2, which are accompanied by significant volume expansions, of about 7.5 ad 50% respectively. Such local phase transformations may induce high local compressive stresses in the newly formed phase, whereas they may reversely tend to create tensile stresses veins in the oxide layer close to the converted nodules. Going towards high temperatures, beyond ca 850°C, phase transitions are also expected in the metal. Furthermore, metal oxygen and hydrogen pick-up, as well as metal creep can no longer be disregarded. This means that the stress generation and release mechanisms are complex, as such not simple to describe. Nevertheless, as far as the growth mechanism is concerned, it is generally accepted that strong compressive stresses contribute to stabilize the tetragonal phase et the M/O interface.[6,7] For the lowest oxide film thicknesses, it is also thought that the periodic transition from slow to fast oxidation rates results from stress relief processes, in the metal through creep, at the M/O interface (development of surface undulations) and in the oxide through film cracking. These different processes each contribute to reduce the in-plane compressive stresses in the vicinity of the M/O interface. For higher thicknesses, the formation of radial cracks also strongly suggests a transition from a mean compressive to tensile stress state within the oxide film. Finally, on a more local scale, interactions between different grains are also to be considered.

To date, a variety of analytical techniques have been employed to analyze the corroded specimens, that were reviewed in Guérain et al.[50] Considered at the sample scale, stresses can be evaluated by macroscopic means such deflection and/or curvature radius measurements of the sample during one-sided oxidation test. Measurements can also be performed using a variety of analytical techniques, including X-ray diffraction, micro-beam synchrotron X-ray diffraction and Raman spectroscopy, that give information on the crystal lattice strain. For different reasons (metal creep, film cracking, ...), both kinds of methods will not necessarily bring the same information. In particular, spectroscopic or diffraction techniques measure lattice strain rather than stress. The residual stresses are then deduced using appropriate material parameters such elastic compliance and stiffness constants or, from case to case, the more macroscopic or “engineering” averaged Young's modulus and Poisson's ratio. As a rule, the elastic constants are highly anisotropic for m-ZrO_2. In most situations, there is a need for qualitative and, if possible, quantitative assessment of stress levels, and for a direct visualization of residual stress fields at the micron or even nanometer scales. Such an information can only be obtained with local probes, and in such a case, stresses are implicitly assumed to be constant within the measurement sampling volume, which in most cases still remains a strong approximation as long as the probe dimensions are higher than the mean grain size of the oxide films.

Due to its known advantages (non-destructiveness, micron lateral resolution, …), Raman spectroscopy has been extensively applied to residual stress evaluations, for semiconducting materials in particular. [51] However, In the most general case, this technique does not directly provide a “stress value”, more precisely a value of the different elements of the stress tensor. This means that a stress distribution model is necessary to interpret line shifts and/or splitting. Such an analysis is usually conducted for single crystalline systems, providing the geometry of the problem,

stress pattern and measurement conditions, is completely known. In this case, experience shows that measurements carried out on single crystals with a fully controlled measurement geometry can give quantitative measurements, in accordance with mechanical modeling. However, this is generally more complex for polycrystalline systems.

In the particular case considered throughout this paper, such mechanical measurements can be tentatively performed from the main and perfectly identified crystalline phase present in the oxide films, *i.e.* from some of the lines of the m-ZrO_2 Spectrum.

5. 2. Background information

Strain is the response of a crystal to an external influence, for example temperature (*T*) or pressure (*P*). It describes the change in shape and size of a physical object relative to an initial, undeformed, reference state. As far as pressure is considered, strain and stress are related according to the generalized Hooke's law:[52]

$$\sigma_{ij} = C_{ijkl}\varepsilon_{kl} \text{ or } \varepsilon_{ij} = S_{ijkl}\sigma_{kl} \qquad (2)$$

or:

$$\sigma_i = C_{ij}\varepsilon_j \text{ or } \varepsilon_j = S_{ij}\sigma_j \qquad (3)$$

adopting Voigt notation, where σ_{ij} (σ_i), ε_{ij} (ε_i) C_{ijkl} (C_{ij}) and S_{ijkl} (S_{ij}) are the stress, strain, stiffness and compliance tensors respectively, here given in the crystal axis reference frame. The Einstein summation convention is applied. The strain tensor does not need to conform to the crystal symmetry when stress is applied in a general direction, meaning that the crystal symmetry may be altered. Strain may also be caused by temperature changes. In such a case, the strain conforms to the crystal symmetry, and is determined from the thermal expansion coefficient tensor.[52] For the monoclinic system, there are 13 independent compliance and stiffness components. For m-ZrO_2, this information is available, from measurements or *ab initio* calculations.[53-55] As one can see here, pure shear deformation causes also normal stresses, since some of the coupling terms are not zero, meaning that pure strain can also result in shear stress. Consequently, the principal orientations of the stress and strain tensor do not necessarily coincide. Any arbitrary stress tensor, applied to a crystal in another arbitrary orthogonal reference frame can be always transformed into an equivalent stress tensor in the crystal reference frame using known rules of coordinate transformations. The thermal expansion tensor possesses four different elements that relate changes in the lattice parameters to temperature changes.[52] The conventional orientation for monoclinic system relative to set of orthogonal reference axes (*X*, *Y*, and *Z*) is *Y//b and Z//c*. The angle between the *a* and *Z* axis is of about 99°.

m-ZrO_2 stiffness coefficients are given in table S1 (Supporting Information). It is seen that the mechanical properties are highly anisotropic. Polycrystalline elastic properties are given as well, see table S2 (Supporting Information). They were obtained averaging the stiffness constants according to known Voigt-Ruess-Hill procedures.[55] Finally, the thermal expansion coefficients, extracted from Pétigny et al.,[56] are given in table S3 (Supporting Information), along with commonly accepted

polycrystalline values for the oxide and the metal. The thermal expansion coefficients are also highly anisotropic.

Because the anhamonicity of the crystal potential, the response of lattice dynamics follows the response of the static lattice to changes in temperature or pressure. Different approaches have been used to relate strain, stress, to Raman shifts, all using the quasiharmonic approximation, which allows the strain dependence of the phonon wavenumbers to be taken into account, but still consider them to be harmonic.

Those different approaches used so far are first to be discussed at the crystal lattice scale, in the range of the validity of Hooke's law.

The first one introduces the so-called Grüneisen parameter. In its microscopic formulation, the Grüneisen parameter $\gamma(q, s)$ is a measure of how a specific phonon frequency $\omega(q, s)$ is altered under a small change in the geometry of the crystallographic unit cell. Here, q is a specific wave vector in the first Brillouin zone and s an index which refers to a specific mode. For isotropic materials, or materials with cubic lattice symmetry, the most commonly discussed situation, the Grüneisen parameter is simply a scalar that refers to an isotropic change in the volume V, according to:

$$\gamma\,(q,s) = -\frac{V}{\omega\,(q,s)}\left(\frac{\partial\omega\,(q,s)}{\partial V}\right)_T = -\left(\frac{\partial \ln \omega\,(q,s)}{\partial \ln V}\right)_T \qquad (4)$$

For such materials, the change in the volume V is simply the trace of the strain tensor.

Introducing the bulk modulus $K = -V(\partial P/\partial V)$, and the compressibility $\kappa = 1/K$, Eq. 4 writes:

$$\gamma\,(q,s) = = -\left(\frac{\partial \ln \omega\,(q,s)}{\partial \ln V}\right)_T = \frac{1}{\kappa\omega\,(q,s)}\left(\frac{\partial\omega\,(q,s)}{\partial P}\right)_T \qquad (5)$$

Note that K is not a strictly a constant, but is *a priori* a function of pressure (P) and temperature (T). If the anharmonicity in the potential is relatively small, the Grüneisen parameter remains approximately constant with either P or T. Then, the mode Grüneisen parameters can be determined under isostatic stress conditions. Usually, the Grüneisen mode parameters are positive and lie in the range 1.5 ± 1. This specific approach was used in Refs[17,57] to determine a stress value in Zircaloy oxide layers.

Nevertheless, the isotropic approach may prove insufficient. As mentioned in Refs.[58,59], the isotropic approach a special case of a more generally defined Grüneisen parameter $\gamma(q, s, \varepsilon_i)$ that expresses how $\omega(q, s)$ varies under a small change in ε_i, where ε_i is a given strain along a specific direction of the unit cell.

$$\gamma\,(q,s,\varepsilon_i) = -\frac{1}{\omega\,(q,s)}\left(\frac{\partial\omega\,(q,s,\varepsilon_i)}{\partial\epsilon_i}\right)_{\varepsilon_j} \qquad (6)$$

As a result, the change in the frequency, $\Delta\omega/\omega$ of a phonon mode in a crystal as a function of a general strain ε is determined by a second-rank symmetric tensor, the phonon mode Grüneisen tensor γ:[59]

$$\frac{\Delta\omega(q,s)}{\omega(q,s)} = \gamma : \varepsilon = \gamma_{ij}\varepsilon_j \qquad (7)$$

Because the mode Grüneisen tensor is a symmetric second-rank property tensor, it is subject to the same symmetry constraints on its component values as other second-rank property tensors, such as the thermal expansion and compressibility tensors.[58,59] For the monoclinic crystal system, for each mode, there are four independent parameters are non-zero namely, γ_{11}, γ_{22}, γ_{33}, γ_{13}, that have different values for pressure conditions that do not alter the monoclinic symmetry. Eq. 7 means that the changes in the Raman peak positions depend on all of the strains in three dimensions experienced by the crystal.

Strain effects may also be described according to the so-called phonon deformation-potential (PDP) formalism, still using the crystal axis reference frame.[60,61] As the elastic constants of solids determine how they deform under pressure, the PDPs give the corresponding change in their zone-center vibrational frequencies. Within the quasi-harmonic approximation, each vibrational mode is associated to a strain-free frequency ω_0 and an effective diagonal force constant matrix $K^{(0)}_{ij}$, which is the second derivative of the crystal potential energy with respect to the mode normal coordinate. Its dimension is determined by the degeneracy of the Raman mode. Here, the effective mass is omitted.

To first order in strain, the change in the force constants ΔK_i of non-degenerated modes under stress/strain is given by a matrix, simply writes:

$$\Delta K_i = K_i - K^{(0)}{}_i = K_{ij}\varepsilon_j \qquad (8)$$

Where K_{ij} are the phonon deformation potentials. For the particular case of the monoclinic structure, there are four independent PDPs for each phonon mode of A_g or B_g symmetry, namely, K_{11}, K_{22}, K_{33}, K_{13}, regardless of the stress or strain pattern which maintain the monoclinic symmetry of the crystal.[62] The secular equation that give the wavenumber shift of the vibrational modes of the strained monoclinic lattice writes:

$$\omega^2 - \omega^2{}_0 \approx 2\omega_0(\omega - \omega_0) \approx 2\omega_0\Delta\omega \approx K_{ij}\varepsilon_j \qquad (9)$$

Because of the proportionality between stress and strain in the elastic regime, and still assuming that any strain or stress leaves the symmetry of the monoclinic unit cell unchanged, Eq. (4) may be simply rewritten as:

$$\Delta\omega \approx a\varepsilon_1 + b\varepsilon_2 + c\varepsilon_3 + d\varepsilon_5 \qquad (10)$$

in terms of strains, or

$$\Delta\omega \approx a^*\sigma_1 + b^*\sigma_2 + c^*\sigma_3 + d^*\sigma_5 \qquad (11)$$

in terms of stress. These deformation potentials are to be treated as parameters to be determined by experiment. However, for crystals of lower than cubic symmetry, the determination of the components of the phonon-mode Grüneisen parameters or of the PDPs for even a single vibrational mode may be difficult to achieve experimentally. It requires different strain states to be imposed on a single crystal, at least four for this specific case, or *ab initio* calculations. It is therefore not sufficient to measure the Raman shifts under hydrostatic pressure, because this generates a single strain state. For m-ZrO_2 these parameters are not known.

However, the general approach described above may be simplified for polycrystalline thin films. As a first attempt to tackle this problem, it is possible to consider the case of fine-grained polycrystalline materials, with an isotropic, *i.e.* a completely random spatial distribution of the crystallite orientations. Here, the diameter of the focused probe is assumed to be much larger than the mean grain dimensions. In this way a "macroscopic" polycrystalline volume is probed, rather than individual crystalline grains. The grains are also assumed to be "large enough" so that any size effects on phonon frequencies can be ignored. Therefore, in the absence of strains, the phonon frequencies are taken equal to those of the corresponding single crystal. In the case of a stressed material, the Raman signal reveals a convolution of the signals emitted by many grains, and an "average spectral shift" can be estimated. At first, one can assume that the stress state is uniform throughout the oxide film, and hence equal to its mean value in each grain, in a way equivalent to the so-called Reuss's hypothesis used to compute averaged effective compliance constants. This approach is rather crude because there is no reason for the stress state to be exactly the same in each grain, but nonetheless it allows the link between stress state and line shift to be made quite simple.

According to these hypothesis, Eq. 6 reduces to:

$$\Delta\omega \approx 1/3\,(a^* + b^* + c^*)(\sigma_1 + \sigma_2 + \sigma_3) \qquad (12)$$

The complete averaging procedure is described in Ma et al.[63] Eq. 12 loses its tensorial character, but maintains a phenomenological meaning. Such an approach is implicitly used in most of the works concerning zirconium oxide layers, see for example Refs.[21,64,65], that use a simple and constant proportionality relationship between line shift and stress.

Accepting these hypothesis, random orientation and a constant mean stress state within each of the grains in the oxide film in particular, Eq. 12 shows that, irrespective of the crystal structure, the wavenumber shift of non-degenerated Raman modes only depends on the trace of the stress tensor, or equivalently to the hydrostatic stress, *i.e.* the average of the three normal stress components of any stress tensor. From this simplified analysis, some limitations stand out. The first one is that a particular line shift of the m-ZrO_2 structure is still insufficient to completely describe the complete stress state. Again, it is still necessary to make some assumptions, a pure biaxial stress state for example. Another consequence is that each of the lines of the Raman spectrum gives exactly the same incomplete information. On the other hand, a simple calibration on a polycrystalline sample is sufficient to extract the coefficient that link wavenumber shift and the hydrostatic part of the stress tensor. Providing that this calibration is carried out under controlled pressure conditions, unlike the XRD-based $sin^2\Psi$ method,[66] a detailed knowledge of the averaged "engineering" elastic constants, *i.e*. Young's modulus and Poisson ratio, is no longer necessary to get stress values.

Obviously, in the case of a pronounced film texture and/or large grain sizes, this simple approach loses its validity. For the oxide layers grown on zirconium alloys, a fibre texture is effectively evidenced.[56,66-68] The axis of the fibre texture, i.e. the crystallographic direction common to a large majority of the grains of the oxide, is close to the c axis of the unit cell.

Raman spectroscopy can therefore only be used semi-quantitatively, to give some orders of magnitude.

5. 3. Thermal stress.

An important additional issue arises from the fact that measurements are performed at room temperature, after cooling from the high temperature oxidation conditions. From a pure mechanical viewpoint, while cooling a sample, thermal stresses add to the stresses that developed during oxidation. A consequence is that stress measurements evaluations are biased, unless performed *in situ*, at the oxidation temperature. Raman spectroscopy may be also a convenient tool to perform *in situ* measurements. However, one prerequisite is to have a reference material in the growth environment, to give the strain-free wavenumbers at the growth temperature of the oxide layer. Even in this case, we believe that the information gain may be quite limited insofar only a the first few µm of the oxide layer are probed. This means that beyond a thickness of a few µm, only this first-formed layer is continuously analyzed, and that the information of the physico-chemical processes that occur at the M/O interface is lost rapidly.

Through a first rough thermoelastic analysis, thermal stresses computation is quite straightforward assuming elasticity and macroscopically isotropic properties for both the metal and the oxide layer, *i.e*. spatially averaged macroscopic Young's modulii, Poisson coefficients and coefficients of thermal expansion. As far as Zircaloys and m-ZrO_2 are concerned, assuming a completely elastic behavior of the layer and its substrate, the ratio of macroscopic CTE values, α_{ox} /α_m exceeds unity, see table S3 (Supporting Information), and some tensile stress must be generated in the scale during cooling of the oxidized systems, according to:[49]

$$\sigma_{ox} = \int_{T_i}^{T_f} \left(\frac{E_{ox}}{(1-\nu_{ox})}\right) \left(\frac{(\alpha_m-\alpha_{ox})dT}{\left(1+{}^{e_{ox}}/_{e_m}\right)\left({}^{E_{ox}}/_{E_m}\right)\left({}^{1-\nu_m}/_{1-\nu_{ox}}\right)}\right) \qquad (13)$$

where *E* are Young's modulii, ν the Poisson's coefficient, α the coefficients of expansion, *e* the thicknesses, and the subscripts *ox* and *m* refer to the oxide and metallic substrate respectively.

Using commonly accepted Young modulus, Poisson coefficient and CTE values (see table S2 and S3 (Supporting Information)) and film thicknesses of a few tens of µm, tensile stresses are expected to be rather low, a few hundred MPa at most, that is to say well below the accepted compressive stresses levels measured from XRD studies that are usually reported to lie in the GPa range.[50] This trend effectively seems to be partially observed from *in situ* XRD measurements, but not in a systematic way however.[48,56] For higher temperature conditions, above 850°C, higher tensile stresses are expected because of the high volume change associated to the β to α Zr phase transition, and the accompanying change in the CTE of the metal.[69] Here the effects of hydrogen and/or oxygen incorporation in the metal should also be taken into account.

Again, this first simple approach is probably insufficient insofar the main phase of the oxide layer is made of a crystallographically, elastically and thermoelastically highly anisotropic and textured material. In particular, the thermal expansion of the zirconia is highly anisotropic and very large differences are observed between the different crystallographic directions, see table S1 and S3 (Supporting Information). Still assuming that the axis of the fibre texture is close to the c axis of the unit cell, the a and b directions more or less lie parallel to the M/O interface. Comparing the different coefficients of thermal expansion measured along the different crystal axis, it becomes clear that, on average, the a direction of the monoclinic structure will be stretched while the b direction will be strongly compressed upon cooling. Because the elastic anisotropy is also very large, the mean deformation of the monoclinic lattice becomes rather difficult to predict. Nevertheless, this is perhaps not a strong issue as long as the thermal stress remains low compared to the growth stress, as it should be the case for temperature conditions close to the in-pile ones. Clearly, the analysis has to be developed in more detail. Nevertheless, this is clearly outside the scope of the present paper.

5. 4. Calibration of the Raman shifts. Results available from the literature.

The literature lists a few works that can be used for calibration purposes. These tests were carried out under isostatic or uniaxial pressure and performed on pure m-ZrO_2 powders and/or sintered pellets. In all cases, the stress dependence of all the peaks of zirconia phases was found to be linear below a certain stress level and the slope of these plots could be extracted.[57,70,71] Under hydrostatic pressure, a phase transition towards an orthorhombic phase was observed at about 3.5 GPa. The main trends, are given in table S4 (Supporting Information), which gathers the pressure derivatives of most of the 15 observable lines of m-ZrO_2. First, it is seen that the two sets of data obtained under isostatic pressure are in quite good agreement, even if the difference between the pressure derivatives can reach about 30%. This is not completely unexpected, such differences were already observed for other materials, silicon for example. They show that the observed bands can be divided into three groups according to their pressure dependence. The first group, which include 11 of the 15 bands, is that which exhibit expected line upshifts with increasing pressures, and some of these bands (for example M1, M5, M12, M14) exhibit rather large pressure dependences. The second group composed of two bands, M4 and M6, stays at a more or less constant wavenumber. The third group consists of two bands, M10 and M11, that shifts towards lower wavenumbers with increasing pressures. As expected, lower pressure derivatives were obtained when measurements were performed under uniaxial stress conditions. According to the polycrystalline model, a ratio of three is expected between the sets of data obtained under isostatic and uniaxial pressure. This is more or less verified for about half of the analyzed lines, those located at low wavenumbers in particular, while for some other lines, this ratio can be very different from 3. Moreover, the strong downshift upon pressure of the M10 and M11 lines was not reproduced using uniaxial stress conditions. These calibration measurements must therefore be considered with caution, but they make it possible to extract a few orders of magnitude from the Raman measurements.

In practice, from all the results available in the literature, the mechanical effects on the lines positions are expected to be weak, a few cm^{-1} at most. They are to be determined from least-square fitting routines. The highest result reliability is obviously obtained fitting strong and isolated lines, such as the relatively sharp M2 and M3 doublet or the M10 line, which are not overlapped with the other lines of the m-ZrO_2 spectrum. However, from polarization measurements,[72] the symmetry of

the M2 mode is still uncertain (A_g +B_g modes with more or less equal frequencies). *Ab initio* calculations effectively predict two modes with very close frequencies but of different symmetry.[38,42,43,73] More, the behavior of the M10 mode under pressure differs according to the calibration procedures, see table S4 (Supporting Information). Again, results must be regarded with some caution.

5 5. Calibration. Need for accurate wavenumber references.

The determination of residual stress by Raman spectroscopy depends on the correct measurement of strain-free material line positions, or alternatively the enforcement of some assumption about the state of strain or stress within a particular area of the sample. The same need for a strain-free material holds when one tries to extract strain values from direct measurements of the lattice parameters from X-ray diffraction patterns. On the other hand, this constraint vanishes when the $sin^2\psi$ method is used, a known and important advantage of this method.

It may represent a rather large uncertainty in residual stress measurements since there are reasons for which the strain-free wavenumbers can vary in ways that are unrelated to stress, as simple laser heating for example. Laser overheating is now easily controlled using modern instruments, which are in essence very bright. Moreover, Raman modes, as well as lattice parameters, may be very sensitive to the presence of alloying elements in cationic substitutional sites, meaning that these alloying effects are to be minimized or even eliminated. As mentioned in the experimental part of the paper, this can be achieved using convenient reference samples, stoichiometric strain-free standards obtained from the complete oxidation of Zircaloys coupons, in the form of powders or film fragments detached from their substrate. The differences in line positions between commercially available powders and these reference samples was indeed found to be significant, of about the same order of magnitude than the information being sought. However, reference samples (powder and film fragments) are not free from micro-strains. Nevertheless, samples from both sources have shown identical Raman shifts within an error margin which has been evaluated to be about +/-0.1 cm^{-1}. Because of the oxide growth mechanism, oxygen sub-stoichiometry is obviously another concern, particularly close to the M/O interface where it is expected to be quite high. A few measurements have been carried out on "black m-ZrO_2" powders produced by annealing m-ZrO_2 reference grains in H_2 at about 1000°C. They did not evidence clear and significant line shifts. Nevertheless, the effect of oxygen sub-stoichiometry is not completely known nor understood both for the reference and oxide films materials, and its effects on line positions cannot be further discussed. Therefore, potential sources of error and uncertainty are quite numerous.

5. 6. Low temperature samples. First observations. Validity of the polycrystalline approach

Both LT and HT oxides, with thicknesses in the 20 - 30 µm range, were examined using these protocols. In what follows, the data are plotted as wavenumber shifts from the unstrained sample reference. This allows an easier reading of the data. The main trends obtained to date are discussed, based on the analysis of a few examples.

As a first step, a particular LT sample is examined. For this particular sample, oxidation was conducted in a static isothermal autoclave operating at 360°C in simulated primary water chemistry, at a pressure of about 155 MPa during 1265 days. The sample effectively exhibited the well-known stratified micro-texture, that corresponds to the one already shown in Fig. 1. The thickness of each stratum was close to 2 µm, the overall oxide layer thickness was about 30 µm.

Simple vertical line scans were examined first. Strong oversampling conditions, *i.e.* a point spacing of 100 nm between two consecutive measurements, were used, as an attempt to bring out some information relative to each stratum. This particular line profile was repeated three times, with different incident powers. Within the experimental accuracy, all three data sets gave exactly the same results in terms of line shifts. Along the line profile, all the individual spectra mostly exhibited the characteristic signature of m-ZrO_2, with only a minor it- and bt-ZrO_2 contribution. In particular, it-ZrO_2 could not be clearly identified along the M/O interface. The analysis of each individual spectrum is thus quite straightforward.

This first simple measurement, as well as all those carried out to date on LT, oxides brings several information.

First, the location of the oxide layer was determined using the integrated intensity of a particular line, or equivalently of the integrated intensity of the whole spectrum, as a function of the vertical position in the sample. Here, we used the integrated intensity of the M2 mode, see the black trace in Fig. 7.a. The mean integrated intensity of this signal, is rather constant throughout the oxide film thickness, within the exception of a thin layer near the M/O interface, for which the intensity drops strongly. This layer has a thickness of a few µm. It corresponds to the last oxide formed, which is most likely sub-stoichiometric. Moreover, as shown in Fig. 7.a., the intensity of this specific mode makes it possible to highlight the stratified nature of the oxide layer, through small intensity oscillations. The period of these oscillation is effectively close to about 2 µm. It is clear that this signal modulation is smoothed by the size of the probe, which is close to one µm, while the size of the circumferential cracks is rather of about a few hundred nm. The detection of such signal intensity modulations nicely reflects the spatial resolution that can be reached, providing the experimental conditions are perfectly stable.

In Fig. 7.a. are also plotted the line shifts of the M2, M3 and M10 modes *vs* their reference positions. The analysis of these line shifts gives several information. First, the observed line shifts are rather weak, always below 2 cm^{-1}, whatever the mode considered. Again, the small modulations of the line shifts may be related to the stratified nature of the oxide layer. Second, considering the isostatic stress-shift coefficients that are given in table S4 (Supporting Information), of about 2, 2.5 and -1.35 cm^{-1}/Gpa for the M2, M3 and M10 modes respectively, it is clear that all three modes do not bring the same information, as it was expected from the simplest random grain orientation hypothesis. They do not evolve consistently along the profile, and do not allow to get a single and constant value of the mean isostatic stress at a particular location in the oxide layer. Moreover, from the evolutions of the M2 and M3 line shifts, even the nature, *i.e.* tensile or compressive, of the stress is not unambiguously determined, in particular in a region close to the M/O interface. The analysis of the other modes (Fig. S4, Supporting Information), the M14 and M15 modes in particular, leads exactly to the same conclusion. Different measurements were repeated for this same sample, that were

completely consistent with the trends described above. Moreover, the same trends were also observed using the line mode of one of our spectrometers, thus averaging the data at a particular vertical position within the layer. Finally, preliminary measurements conducted on samples oxidized for different temperature and atmosphere conditions, or of other alloy compositions, also point in that direction. This means that this simplified model is most probably inadequate, and that the use of a single Raman mode as a strain or stress gauge may lead to erroneous conclusions. For all these reasons, the line shifts have not been translated in terms of corresponding stresses.

The corresponding M2 line intensity, M2, M3 and M10 line shifts images are given in Fig.7.b-e, respectively. This particular Raman image was recorded elsewhere at the sample. The sample was examined over a distance of 50 µm, with a measurement step of 0.7 µm in both x and y directions. Despite the higher sampling step, the stratified microtexture is still recognized in the M2 mode intensity image. The contrast of the line shift images always remains relatively low, lower than 0.5 cm^{-1} for the M3 and M3 modes, lower than 1.5 cm^{-1} for the M10 mode. From these images one can extract and visualize horizontal and vertical profiles. The examination of the vertical profiles leads to the preliminary findings, already described above. The horizontal profiles (not shown here), also exhibit some fluctuations, that are to be related to micro-strains, as discussed below. These line shift fluctuation are rather weak for the M2 and M3 modes, about + /- 0.2 cm^{-1} at most, on both sides of an average value. They appear to be slightly more important for the M10 mode, especially in the lower part of the oxide layer, close to the M/O interface, reaching +/- 0.4 cm^{-1}. For this spatial resolution, close to 1 µm, the average micro-strain in the sampling volume therefore remain moderate. For M2 and M3 modes, this average line shift values remain almost constant throughout the thickness of the layer, within the exception of an area of a few microns of thickness, located near the M/O interface. In no case those line shift images allow the identifications of grain columns, or even group of grains. This is perhaps not surprising given the small grain size of the oxide layer, much lower than 100 nm, and the strong porosity. Finally, the line-width images do not give any particular contrast, still within the exception of an area close to the M/O interface, where the line widths were slightly higher.

Interestingly, it was possible to discriminate between samples of different thickness, or samples obtained for different alloys. However, the differences were always weak.

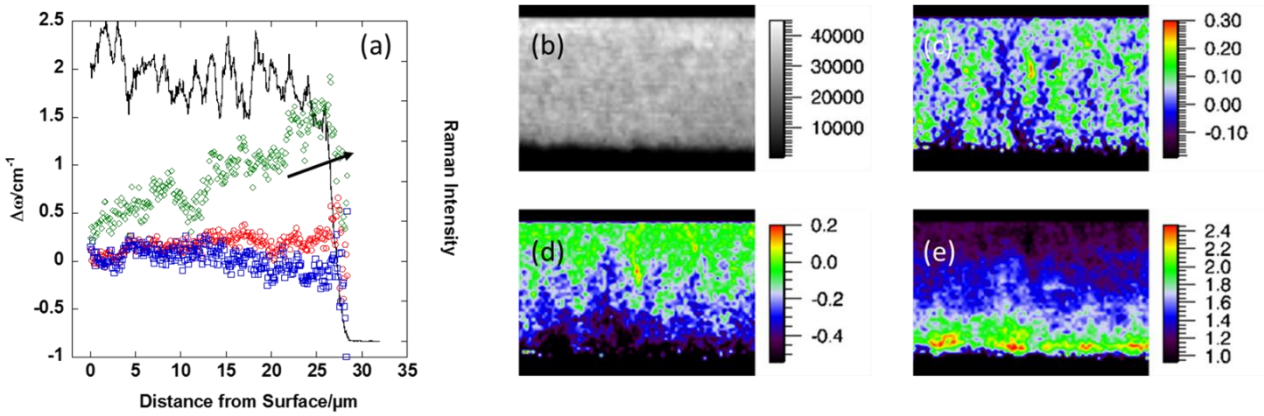

Figure 7: *Sample oxidized in a static isothermal autoclave operating at 360°C in simulated primary water chemistry, at a pressure of about 155 MPa. (a): line scan along the film thickness. Dark trace:*

integrated intensity of the M2 mode. Red circles, blue squares and green diamonds: line shifts of the M2, M3 and M10 modes vs a reference, strain-free sample. Right: corresponding images: (b), integrated intensity of the M2 mode (Arbitr. Units), (c), (d) and (e): line shifts of the M2, M3 and M10 modes respectively (cm^{-1}). The sample was analyzed over an area of 50 x 36 µm.

5. 7. High temperature samples - Macro- vs micro-strain

We now focus on the examination of layers formed at a higher temperature, of more or less equivalent thicknesses. In the pre-transition protective regime, these layers are expected to be dense, mostly micro-cracks-free. It is therefore expected that the mechanical properties of such layers should be rather different from the one of layers formed at lower temperatures, which, as we have just seen, are characterized by a typical stratified microstructure along with a network of circumferential micro-cracks parallel to the M/O interface. Therefore, mechanical stress relaxation phenomena are expected to be weaker.

For the specific specimen examined here, oxidation tests were performed in a mixed N_2 - O_2 - H_20 atmosphere, the substrate was a Zy-4 plate. The O_2 fraction in the oxidizing atmosphere was about 30%, the growth temperature was 850°C. In contrast to what was observed for the LT samples, simple vertical line scans from the film surface to the M/O interface never gave consistent results in terms of line shifts. The examination of the Raman images allowed to provide more insight and to understand the origins of this lack of reproducibility.

The sample was analyzed over an area of 140 x 17 µm, with a point spacing of 0.7 µm in both directions. We still focus on the evolution of M2, M3 and M10 modes. The corresponding images are given in Fig. 8.b-d., along with the tetragonal phase distribution image (Fig. 8.e) that was detected along the M/O interface. The overall appearance of these images is quite typical of those obtained above 800°C, more or less independently of the composition of the oxidizing atmosphere.

The M2 line intensity images (not shown here) did not reveal any particular contrast. On the whole, the signal remains of low intensity, only exhibiting a trend to higher intensities close to the gas/oxide interface. Again, this can be understood in terms of oxygen hypo-stoichiometry, which is confirmed by the black color of the oxide layer.

In a first reading, the contrast of the 3 line shift images, in particular the local contrast, is greater, close to 1 cm^{-1} or more. Throughout the thickness of the layer, the 3 images seem to identify groups of grains. For the three modes, the highest line upshifts are observed along the M/O interface. t-ZrO_2 seems to be observed in regions where the upshift are the most important, but this cannot be completely generalized for all the samples examined to date. At this point, a first and rather important conclusion is that a single point measurement definitely cannot describe the oxide layer.

To go further in the description of the measurements, it is possible to extract horizontal wavenumber shift profiles from the images, and/or to obtain average information for a given thickness in the oxide layer. The analysis of the horizontal wavenumber shift profiles is expected to give relevant information on the micro-stresses, while the average data can be rather related to macroscopic stresses. Another interesting data is the standard deviation of the line shift values along a specific

line, which is to be related to the micro-contrast, *i.e.* the dispersion of the line shifts around the mean value for a given height in the layer.

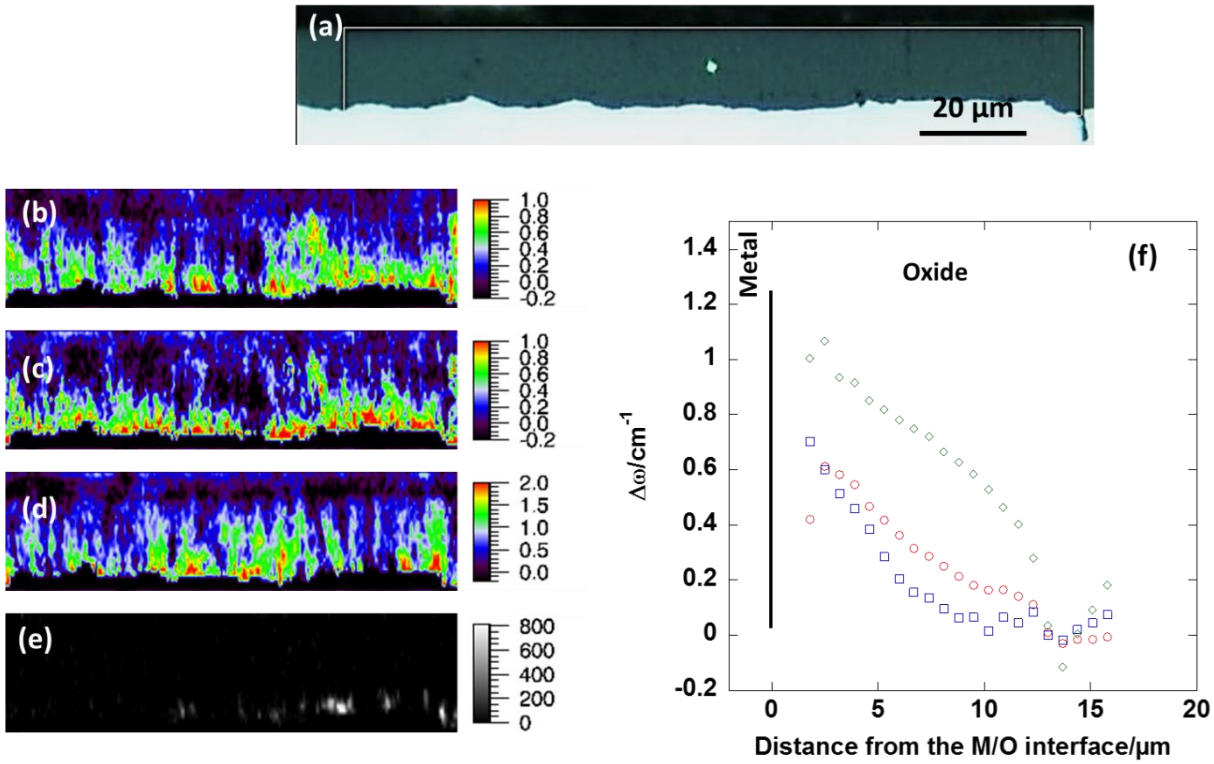

***Figure 8**: Sample oxidized in a mixed N_2 - O_2 - H_20 atmosphere. The O_2 fraction in the oxidizing atmosphere was about 30%, the growth temperature was 850°C. The sample was analyzed over an area of 140 x 17 µm. (a) Optical image. Raman images of the line shifts of the M2 (b), M3 (c) and M10 (d) modes vs a reference, strain-free sample (cm^{-1}), and (e) it-ZrO_2 phase distribution (Arbitr. Units). The Y axis of the Raman images is not to scale, to highlight the columnar-like appearance of the oxide layer. (f): Red circles, blue squares and green diamonds: line shits of the M2, M3 and M10 modes vs a reference, strain-free sample. The line shifts were obtained averaging the data along horizontal profiles, at a given distance from the M/O interface.*

Here, the mean line shift and standard deviation values are obtained on a distance of 140 µm, wide enough for the calculated values to be representative of the sample. As before, the line shifts were obtained from the comparison with the reference material. Fig. 8.f. shows that the averaged line shifts evolve very regularly from the M/O interface towards the sample surface. As more or less expected for this specific case, the highest upshifts are found close to the M/O interface, an indication of compressive stresses on average. The proposed method therefore seems to make sense, and indeed give some average information. The line shifts always remain moderate, lower than ca 1 cm^{-1} for the M10 mode, than 0.6 cm^{-1} for the M2 and M3 modes. Again, the evolution of the line shifts does not correspond exactly to the one predicted by the polycrystalline model, nor the isostatic model, especially since the line shifts of the M2 and M3 modes remain mostly similar. Fig. S5 (Supporting Information) also shows that the standard deviation decreases strongly from the M/O interface to the gas/oxide interface. Again, the evolution is very gradual, and is similar for all three

modes, which may be an indication that the micro-deformations are relaxing in the upper part of the oxide layer. This relaxation can first correspond to the creation of micro- or nano-porosity.

In this analysis, the undulation of the M/O interface must also be considered. Indeed, we expect to observe locally different states of stress, rather a tensile state above the convex parts and a compressive state above the concave parts of the M/O interface. Such stresses were effectively predicted to progressively relax in the upper part of the oxide layer.[66] Nevertheless, considering Fig. 8, this is not what seems to be clearly observed here. The reading of the individual horizontal profiles does not give further information.

If we accept here this interpretation of line shifts in terms of residual stress only, it seems also important to mention that local stresses, at least at the µm scale, are more important than long range stresses, which of course must have strong consequences on the mechanical strength of the oxide layer.

For this specific example, t-ZrO_2 was indeed detected in the form of isolated spots along the M/O interface, see Fig. 8.e. However, it was not possible to obtain a strict correlation between line upshift (therefore compression), and the presence of t-ZrO_2.

5. 8. Current findings

To date, several LT and HT samples have been examined with the protocols described above. Most of the results presented above can be generalized. Therefore, the different line shift images do contain information. Nevertheless, it is difficult to give a clear quantitative interpretation of these data. This raises the question of the exact meaning and value of the “stresses” deduced from the line shifts. For different reasons, this is still an open question.

First, the state of the unstrained material is still not known with certainty, meaning that special care should be taken in assessing the corresponding stress-free peak position for a selected mode. The lattice parameter of some oxides, *e.g.* actinides oxides, is known to vary quite strongly with oxygen hypo- or hyper- stoichiometry. In the present case, no clear data are available for monoclinic zirconia. Moreover, as already mentioned, Raman modes, as well as lattice parameters, may be very sensitive to the presence of alloying elements in cationic substitutional sites, meaning that these alloying effects are to be minimized or even eliminated.

Second, the only working hypothesis that allows to get orders of magnitude of a “stress” level is the isotropic or polycrystalline approximation, referring to calibrations conducted under controlled isostatic stress. This approximation does not give all the individual components of the stress tensor, but only its trace. This hypothesis, by far too restrictive, suggests that residual stresses, measured at room temperature, remain moderate, probably below ca 1 GPa. This first order of magnitude corresponds more or less to those usually obtained by X-ray diffraction.[50] Again, in standard X-ray diffraction procedures, the material is considered to be homogeneous and isotropic. Lattice strains are assumed to be homogeneous in the analyzed diffracting volume. They are measured with no depth resolution and are averaged over the whole oxide layer. There is no obvious reason why the average stress should be purely isostatic. This is why most of the X-ray diffraction work assume a

biaxial stress. Even this second assumption in itself still seems too restrictive. As a matter of fact, recent studies[34,35] using X-ray micro-diffraction suggest that the monoclinic lattice is far from being homogeneously deformed. Some of those spatially-resolved studies have shown that both in-plane and through-plane stresses exist in the oxide for films of 1 µm and thicker, with compressive in-plane and tensile out-of-plane components. When measured at room temperature, in-plane and out-of-plane components may have similar amplitudes, around 500 and -500 MPa respectively. Again, these values were extracted using averaged mechanical properties.

Third, it seems clear that none of the methods used so far takes into account the texture of the oxide layer, and the strong anisotropy of the thermal expansion and stiffness coefficients of m-$Zr0_2$. Using Raman spectroscopy, this problem cannot be solved without the knowledge of the material PDPs.

All these considerations show that what is currently determined by the methods is not bulk stress, but, as mentioned in Pétigny et al.,[56] rather "pseudo-stresses", whose absolute values are questionable, but whose temporal or spatial evolution can be considered, though cautiously. Clearly, this analysis deserves to be developed in more detail.

6. Using labelled oxygen during the oxidation tests

Isotope substitution is known to be a unique tool for distinguishing different Raman active modes, and can lead to reliable mode assignments. In addition, this isotopic labeling technique can be used to obtain other information, for example to study complex reaction mechanisms in the field of catalysis, or to understand and quantify transport phenomena in solids. Two-stage oxidation experiments using isotopes as diffusion tracers are effectively known in the corrosion community to give valuable inputs on diffusion processes during oxidation, and their use has extensively been reported for various metallic systems.[74] First, the use of the ^{18}O isotope allows discriminating between anionic, cationic or mixed anionic + cationic transport mechanisms involved in formation of protective thermally grown oxides.[75, 76] Second, the analysis of the ^{18}O in-depth diffusion profiles allows the determination of the oxygen bulk and/or grain boundary diffusion coefficients.[14, 76, 77]

More, isotope labelling technique may be used to unravel the reaction mechanisms and the transport processes in complex atmospheres, for example containing both air and steam, by marking one of the oxidizing species. In this last case, the whole experimental protocol has to be designed to prevent or limit gas phase isotopic scrambling.[78]

Secondary Ions Mass Spectroscopy (SIMS) is most often the technique used to track the isotope distribution in the oxide layer after the oxidation tests.[74,76,77] Nevertheless, even if rarely used for such a purpose, micro-Raman spectroscopy is another technique which is able to extract ^{18}O profiles in the oxide layers. As a vibrational spectroscopic technique, this method indeed provides a mass contrast. ^{18}O profiles can then be related to the structural and mechanical properties of the oxidation layer, or even, as described below, to some reaction mechanisms.

6.1. Consequences of oxygen isotopic substitution on the m-ZrO_2 spectrum

For the range of experimental conditions considered herein, m-ZrO_2 is always the predominant crystallographic phase. This means that the local isotopic composition can be extracted from its corresponding Raman spectrum. As already described, within the framework of the harmonic approximation, the frequency of each zone-center Raman-allowed mode is proportional to $\sqrt{K_i\ /\mu_i}$, where K_i is an effective force constant and μ_i an effective mass.[45] The effective force constant brings structural information, while the effective mass naturally brings chemical or isotopic information. The virtual crystal approximation is usually introduced for a crystal containing several isotopes in order to recover the translational invariance lifted by the isotopic disorder, meaning that masses of these isotopes are simply replaced by their average weighted relative abundances.

A precise analysis of the isotopic effect requires the knowledge of the effective masses of each normal mode. However, for our purpose, it is sufficient to make rough estimates based on the limiting cases of Zr- or O-dominated modes, either referring to the partial VDOS available from the literature,[42-44,73] or more simply to known calibration results which consist in synthesizing reference standards of several compositions.[79,80] In both cases, O-dominated are found in the high wavenumber range of the spectrum, schematically above ca 400-450 cm^{-1}, see table S4 (Supporting Information). In this wavenumber range and according to this approximation, the shift induced by oxygen isotopic substitution for each of the Raman modes characteristic of m-ZrO_2 can be estimated according to:

$$\frac{\omega_i(Zr^{18}O_2)}{\omega_i(Zr^{16}O_2)} \sim \sqrt{\frac{\mu(^{16}O)}{\mu(^{18}O)}} \qquad (14)$$

where $\mu(^{16}O)$ and $\mu(^{18}O)$ are the masses, $\mu(^{18}O)$ the mass calculated using the actual atomic percentage of ^{16}O and ^{18}O in the samples, ω_i *(*$Zr^{16}O_2$*)* and ω_i *(*$Zr^{18}O_2$*)* the corresponding mode frequencies. Here the 0.2 % natural abundance of ^{18}O can be neglected.

In practice, the M10 mode, peaking at 475 cm^{-1} for the oxygen natural isotopic abundance, intense and isolated from the others, can be used for quantitative detection of ^{18}O in zirconia layers. As shown in different works,[79,80] the line downshift versus the ^{18}O content is strong, estimated and measured to be about 0.27 $cm^{-1}/^{18}O$ at.%. Nevertheless, the M10 line contains *a priori* two information, *i.e.* mass and strain, which obviously introduces some uncertainty in the extraction of the ^{18}O content. This uncertainty has been discussed in Mermoux et al.[78] and was estimated to be about 5 at% at most. Because of the possible strain contribution, the Raman-based method likely has a significantly higher detection threshold than SIMS (less than 1%) for oxygen isotopic analysis. Nevertheless, in the high ^{18}O concentration range, it has been shown that Raman and secondary ion mass spectroscopy (SIMS) concentration images compared well, spatially as well as quantitatively.[81]

Again, it is necessary to keep in mind that ^{18}O concentration estimates are averaged values within the probing spot (about 2 μm^3). Indeed, in the oxide layers, the grain size was found to lie between a few tens and a few hundred µm from SEM/FEG images. Such a probed volume obviously contains a high number of Zirconia grains. Because it was already shown that diffusion along the grain boundaries

was much faster than in-grain diffusion, ^{18}O concentration gradients within individual grains may be expected.[79]

6.2. Oxygen transport. Two stage oxidation experiments.

The purpose of two stage oxidation experiments is usually to gain information on solid-state oxygen transport within the zirconia scales. Therefore, they are to be performed in the so-called protective regime, in which the oxidation process is known to be driven by inward solid state diffusion of oxygen through the growing zirconia scale. Again, such a macroscopic information is usually available from the thermogravimetric records. Accordingly, the mapped areas are to be chosen far from the samples edges, in regions where the oxide layer is still apparently dense and crack-free.

The particular two-stage oxidation experiment described below was performed by oxidizing a zircaloy-4 cladding sample at 850°C, in $H_2{}^{16}O$ during 30 min, then in $^{18}O_2$ atmospheres during 60 min. To minimize the uncertainties on the isotopic composition, high purity (97%) $^{18}O_2$ was used during the second oxidation stage. The sample was not cooled between the two steps of the oxidation test to avoid thermal shocks, which could provoke cracks in the oxide layer. As measured from the optical image, the mean thickness of the oxide layer formed after the two oxidation steps was about 15 µm. ± 2 µm undulations of the M/O interface were also observed. A 400 µm wide area has been mapped out with a point spacing of 1 µm. The isotopic composition map is given in Fig.9.b, along with the M10 mode line width image. Different profiles were extracted from the composition and line width maps, see Fig. 9.c. and Fig. S6 (Supporting Information). The horizontal profiles were extracted in the higher and lower parts of the oxide layer, at about 5 µm from the M/O and gas/oxide interfaces. The vertical one was obtained by averaging 20 individual profiles randomly extracted from the ^{18}O concentration image. Reading these profiles allows a closer description of the results.

The examination of Fig. 9 immediately brings different information.

First, the averaged vertical profile as well as the overall ^{18}O concentration image agree with a growth mechanism that involves inward solid state diffusion of oxygen through the zirconia layer. A progressive exchange of ^{16}O by $^{18}0$ in the first formed oxide allows to understand the concentration profile. Such averaged concentration profiles can be used to determine a macroscopic, or apparent diffusion coefficient, according to more or less sophisticated models.[82] In this particular case, the values deduced from the fit of the diffusion profiles match those obtained by other methods, the oxidation kinetics in particular. The analysis of the diffusion profiles is fully described elsewhere.[82]

Second, the M10 mode linewidth image immediately exhibits unexpectedly high values, locally higher to ca 30 cm^{-1}. This is particularly clear in the vicinity of the gas/metal interface. One can also find such regions within the oxide bulk, much more locally however. These values are by far much higher than those that can be observed for m-ZrO_2 standards obtained for similar ^{18}O contents. In most cases, the line profiles are strongly asymmetric, reflecting ^{18}O concentration gradients in the ~2 μm^3 volume probed. The most probable source for this non-uniformity is a concentration gradient between the grain boundaries and the core of the grains, with the highest ^{18}O concentration in the grain boundaries. Thus, this observation strongly suggests a preferential diffusion path along the grain boundaries. Referring to the classification of diffusion regimes for fine-grained material proposed in

Mishin et al.,[83] these data tend to indicate that the oxygen diffusion regime in the scale is of type B_2', *i.e.* that $s\delta/2 << (D_{bulk}t)^{1/2} << d << (D_{GB}t)^{1/2}$, where D_{bulk} and D_{GB} are the bulk and grain boundary oxygen diffusivity respectively, t the time, d the mean grain size, s the oxygen segregation factor at grain boundary and δ the grain boundary width. Again, a simplified modelling of the tracer profiles confirms that the diffusion coefficients along the grain boundaries are several orders of magnitude higher than the intra-granular ones.[82] Nevertheless, these data still allow a macroscopic interpretation of the transport data.

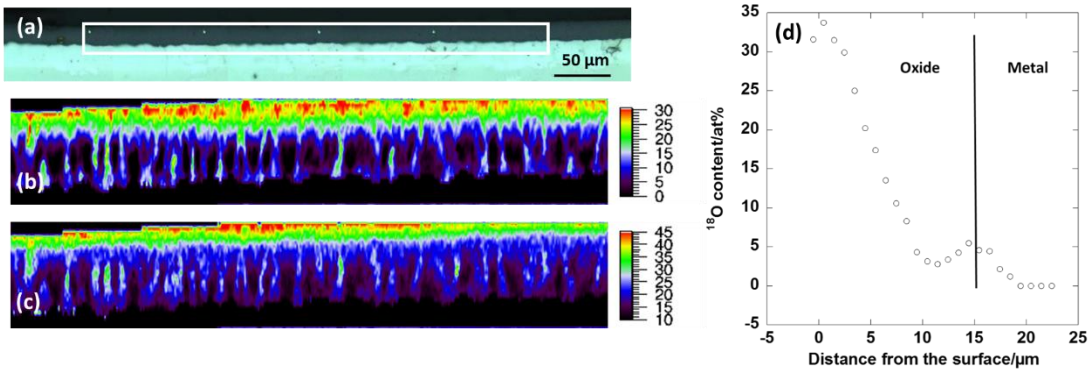

***Figure 9**: Sample oxidized at 850°C, in $H_2{}^{16}O$ during 30 min, then in $^{18}O_2$ atmospheres during 60 min. The sample was analyzed over an area of 400 x 25 µm. (a) Optical image, (b) ^{18}0 content (at%) and (c) M10 mode line width (cm^{-1}) images. (d): mean ^{18}O content profile along the film thickness, obtained by averaging 20 individual profiles at different positions within the oxide layer. The Raman images are not to scale in the y direction, to highlight the local contrast.*

Finally, at a more local scale, both ^{18}O concentration and M10 mode line width images are very inhomogeneous. More, the two images are quite perfectly correlated. They clearly show that ^{18}O may locally reach the M/O interface: ^{18}O contents as high as 25% can observed in these regions, a value close to the one observed near the surface of the oxide layer. Thus, both images reveal numerous diffusion short-cuts, that are to be related to preferential diffusion pathways, or perhaps more simply to the formation of an open micro- or nanoporosity in the oxide layer. Such an open porosity was undetectable with simple optical microscopy. Thus, this ^{18}O concentration image clearly reveals numerous parallel diffusion paths, bulk and grain boundaries and most probably nanoporosity. Some recent measurements suggest that the formation of such an open porosity strongly depend on the alloy composition.

The slight increase of the average ^{18}O content close to the M/O interface is another sign that ^{18}O reach the M/O interface, see Fig. 6.d. This is also clearly evidenced in figure S6 (Supporting Information), see in particular the red trace corresponding to an horizontal profile extracted from the composition image in the vicinity of the M/O interface. The mean^{18}O content is seen to be rather weak. Nevertheless, locally, the ^{18}O content may reach values as high as 20%, or more.

6.3. Oxidation in mixed steam – air atmospheres

Another situation for which isotopic labeling may be of interest is that of a mixed oxidizing mixture, such as, for example containing air and steam. Such a situation is effectively considered in most of

accidental scenarios. Such scenarios are generally only rarely studied, and obviously, the question of the respective contribution of oxygen and steam arises, both in the pre- and post-transition, nitrogen-"catalyzed" regimes. Here, isotopic labelling experiments can be considered, marking one of the oxidizing molecule, either di-oxygen or steam. From an experimental point of view, it is mandatory to ensure that isotopic scrambling in the gas phase catalyzed by any hot surface in the sample growth environment is limited. This means that dynamic rather than static gas flow conditions are to be preferred, to continuously renew the atmosphere seen by the sample. Here, to avoid excessive ^{18}O marked gas consumption, rather low flow rates (about 100 ml/min) were used.[78] This also means that the oxidizing atmosphere has to be monitored in real time, using mass spectroscopy (MS) for example.

As described in Mermoux et al.,[78] oxidation tests were performed in mixed N_2 - $^{18}O_2$ - $H_2{}^{16}0$ atmospheres. Again, to discriminate between the respective contributions of steam and oxygen, high purity (97%) $^{18}O_2$ had to be used. For the particular example described below, the ^{18}O fraction in the oxidizing atmosphere was about 30%. The growth temperature was 850°C, the oxidation duration was 60 min. Gas phase MS monitoring showed that its composition evaluated at the thermobalance exhaust was always close to that initially targeted, meaning that no strong isotopic scrambling occurred in the gas phase in the furnace hot zone. Thus, under the specific conditions used here, ^{16}O and ^{18}O in the ZrO_2 layers essentially or even nearly exclusively derive from steam and molecular oxygen respectively. The isotopic ratio in the scales must therefore give insights on the growth mechanisms.

To analyze simultaneously pre- and post-transition areas, some of the Raman images were recorded close to samples edges. In this case, the expected phases are in all respects similar to those described in Fig. 4, which was effectively the case from the reading of the individual spectra. In these regions, both a dense oxide scale, which formed during the pre-transition regime, and a much more porous post-transition area, which grew later below the pre-transition scale, coexist, see Fig. 10.a. In the optical image, one easily identifies ZrN, which appears in the form of nodules of golden color. Likewise, it is clearly identified on the Raman image (not shown here), the ZrN distribution map perfectly corresponds to the distribution of the golden nodules. The analysis protocol is in all respects similar to the one described above, the ^{18}O content is computed from the line shift of the M10 mode.

The ^{18}O concentration image immediately shows strong contrasts, exhibiting two different regions, of low and much higher ^{18}O contents, see Fig. 10.b. Obviously, the regions of low ^{18}O concentration correspond to pre-transition areas, *i.e.* the first-formed oxide. This was systematically observed for different samples oxidized between 700 and 850°C, and for two different gas phase compositions.[78] The examination of the individual or even the average spectra showed that the measured M10 line downshifts were systematically much lower than ca 2 cm^{-1}, translating ^{18}O contents much lower than ca 10%. In this case, the local ^{18}O content can no longer be determined with accuracy, insofar the consequences of the isotopic and mechanical effects are of a same order of magnitude, leading to line shifts lower than a few cm^{-1}. Nevertheless, in the pre-transition regime for which the ZrO_2 growth process is mostly driven by oxygen solid-state diffusion through the oxide, one important conclusion is that in mixed atmospheres containing the two oxidizing species, the zirconia layers mostly form from steam. Surface reaction steps, including the dissociative adsorption of the oxidizing

molecules at the surface of the different interfaces that are accessible to the gas phase, likely control the competition between oxygen and steam, and the high selectivity between the two oxidizing species. From pure thermodynamic arguments, an opposite conclusion was expected.

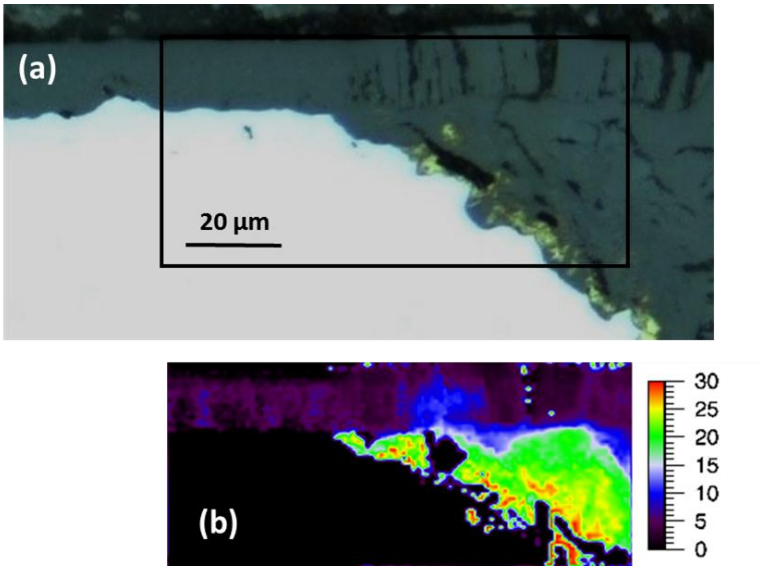

***Fig. 10**: Sample oxidized at 850°C in a mixed N_2 - $^{18}O_2$ - $H_2{}^{16}O$ atmospheres. The ^{18}O fraction in the oxidizing atmosphere was about 30%. The sample was analyzed over an area of 100 x 49 µm. (a): Optical image. (b): corresponding ^{18}O concentration image (at%). Pixels for which ^{18}O content is meaningless (ZrN, Metal, …) have been removed from the original data file. Partially redrawn from Ref. 78.*

On the other hand, in the porous oxide characteristic of post-transition area, the ^{18}O concentrations were more inhomogeneous. In this region, the ^{18}O uptake approaches or even matches the nominal isotopic ratio in the gas phase. Here, the interpretation is less straightforward. This observation can be first understood assuming that the contribution of di-oxygen and steam to the oxidation process correspond to their respective concentrations in the gas phase. Nevertheless, this conclusion cannot be accepted unreservedly. Considering that the porous solid cannot be considered as inert with respect to gas transport, strong recombination in the gas phase may be expected in the open porosity. The main consequence is that both steam and di-oxygen might reach a same isotopic composition, equal to that initially targeted. In such a case, the contribution of both molecules to the oxidation process can no longer be distinguished.

These results are fully described in Ref. 78. Again, preliminary measurements tend to show that these findings are to be modulated according to the composition of the alloy.

7. Concluding remarks

Throughout this paper, we attempted to summarize the use of Raman imaging for the analysis of the oxidation of a particular alloy used in the nuclear industry as cladding materials in light-water reactors. Both normal, in service, and accidental simulating temperature and atmosphere conditions were considered. From a methodological point of view, Raman imaging effectively appears as a

versatile, user-friendly technique, that allows to examine samples over wide dimensions. For this specific case, it appears that data can be analyzed in different ways. In particular, one of the advantages of the method is that a large amount of data is available, allowing it to be examined from purely statistical points of view. At present, this is undoubtedly one of the strengths of the method.

From a more academic point of view, it seems clear that the method can bring, in a single sample scan, structural, mechanical as well as kinetic information through the use of labelled gases in the reactive atmosphere. Some of this information is only qualitative (presence or absence of a phase, residual stresses, ...), but allows to describe the samples at the µm scale. Different algorithms allow to analyze the data sets in order to extract the present structural phases. In this particular case, three different methods converged towards a same sample description. Still in this particular case, it appears that the layers formed at high temperature are probably incompletely described by other techniques, X-ray diffraction in particular. It also appears that the current purely "mechanical" description of the samples seems insufficient. In our opinion, this is partly due to the low symmetry of the monoclinic structure, and the high anisotropy of its thermal and mechanical properties. Finally, using isotopically labeled gases in the oxidizing atmosphere, Raman imaging effectively allows to obtain quantitative data on the oxygen transport in the layers. One can thus visualize quickly several parallel diffusion or penetration paths (grains, grain boundaries, open porosity, ...).

In most cases, the analysis of the results shows that a simple averaged measurement, or even a simple line scan in the samples, does not allow to describe them completely. Interestingly, preliminary results, not described in this paper, tend to show that one can discriminate the oxide layers formed on different alloys. This work is currently in progress.

Still for the particular system considered here, one out of the main perspectives is obviously the examination of samples extracted from nuclear power plants. At present, technical solutions have been developed in several laboratories that effectively allow the examination of such highly radioactive samples. Here, it appears that Raman imaging it is one out of the rare methods that can be used to determine the effects of irradiation on the oxide characteristic features.

Finally, Raman spectroscopy was already known to be a powerful tool to investigate, at the micron scale, other corroding systems. Raman imaging is undoubtly one out of the versatile tools to go much deeper in the analysis of these complex systems.

Acknowledgments.

Throughout this paper, we have used results from different works that involved PhDs and post-docs. We would like to thank Isabel Idarraga, Mathieu Guérain and Anne Kasperski who were involved in some of the measurements and interpretations presented here, and paved the way for writing this this paper. Part of this work has been performed in the frame of the DENOPI project, funded by the French government as part of the “Investment for the Future” Program, reference ANR-11-RSNR-0006. We warmly thank the whole DENOPI consortium for motivating and fruitful discussions.

Supporting Information.

Orcid

Michel Mermoux : https://orcid.org/0000-0002-0108-2197

Christian Duriez : https://orcid.org/0000-0002-2291-9603

References.

[1] M. Delhaye, P. Dhamelincourt, *J. Raman Spectrosc*. **1975**; *3*, 33.

[2] L. Markwort, B. Kip, E. Da Silva, B. Roussel, *Appl. Spectrosc*. **1995**; *49*, 1411.

[3] S. Schlücker, M. D. Schaeberle, S. W. Huffman, I. W. Levin, *Anal. Chem.* **2003**; *75*, 4312.

[4] A. Zoubir (Ed.) *Raman Imaging. Techniques and Applications*, Springer Series in Optical Sciences, **2012**.

[5] G. Koch, in: *Trends in Oil and Gas Corrosion Research and Technologies*, Book Series: Woodhead Publishing Series in Energy, pp. 3-30, **2017**.

[6] A.T. Motta, A. Couet, R. J. Comstock, *Annu. Rev. Mater. Res.* **2015**; *45*, 311.

[7] Cox, B, *J. Nucl. Mater.* **2005**; *336*, 331.

[8] H.M. Chung, *Nucl. Eng. Technol.* **2005**; *37*, 327.

[9] M. Steinbrück, S. Schaffer, *Oxid. Met.* **2016**; *85*, 245.

[10] M. Steinbrueck, F. Oliveira da Silva, M. Grosse, *J. Nucl. Mater.* **2017**; *490*, 226.

[11] C. Duriez, T. Dupont, B. Schmet, F. Enoch, *J. Nucl. Mater.* **2008**; *380*, 30.

[12] C. Duriez, O. Coindreau, M. Gestin, A. Kasperski, V. Peres, M. Pijolat, H. Buscail, C. Issartel, R. Rolland, M. Mermoux, *J. Nucl. Mater.* **2019**; *513*, 152.

[13] T. E. Doyle, J. L. Alvarez, *Raman and Luminescence Spectroscopy of Zirconium Oxide with the Use of the Mole Microprobe*. In: Snyder R.L., Condrate R.A., Johnson P.F. (eds) Advances in Materials Characterization II. Materials Science Research, vol 19. Springer, Boston, MA, pp. 155-165, **1985**.

[14] J. Godlewski, J. Gros, M. Lambertin, J. Wadier, and H. Weidinger, *Raman Spectroscopy Study of the Tetragonal-to-monoclinic Transition in Zirconium Oxide Scales and Determination of Overall Oxygen Diffusion by Nuclear Microanalysis of* ^{18}O, in Zirconium in the Nuclear Industry: Ninth International Symposium, ed. C. Eucken and A. Garde (West Conshohocken, PA: ASTM International, pp. 416-436, **1991**.

[15] H. G. M. Edwards, D. A. Long, I. T. Willis, *J. Raman Spectrosc.* **1995**; *26*, 757.

[16] P. Barberis, T. Merle-Méjean, P. Quintard, *J. Nucl. Mater.* **1997**; *246*, 232.

[17] J. Godlewski, P. Bouvier, G. Lucazeau, L. Fayette, *Stress Distribution Measured by Raman Spectroscopy in Zirconia Films Formed by Oxidation of Zr-Based Alloys*, in *Zirconium in the Nuclear Industry: Twelfth International Symposium*, ed. G. Sabol and G. Moan (West Conshohocken, PA: ASTM International), pp. 877-900, **2000**.

[18] P. Bouvier, J. Godlewski, G. Lucazeau, A Raman study of the nanocrystallite size effect on the pressure–temperature phase diagram of zirconia grown by zirconium-based alloys oxidation, *J. Nucl. Mater.* **2002** ; *300*, 118.

[19] I. Idarraga, M. Mermoux, C. Duriez, A. Crisci, J. P. Mardon, *Oxid. Met*. **2013**; *79*, 289.

[20] J. J. Liao, Z. B. Yang, S. Y. Qiu, Q. Peng, Z. C. Li, J. S. Zhang, *J. Nucl. Mater.* **2019**; *524*, 101.

[21] C. M. Efaw, J. L. Vandegrift, M. Reynolds, S. McMurdie, B. J. Jaques, H. Q. Hu, H. Xiong, M. F. Hurley, Nucl. Mater. Energy **2019**; *21*, 100707.

[22] C. M. Efaw, J. L. Vandegrift, M. Reynolds, B. Jaques, H. Q. Hu, H. Xiong, M. F. Hurley, *Corros. Sci.* **2020** ; *167*, 108491.

[23] M. Gestin, M. Mermoux, O. Coindreau, C. Duriez, M. Pijolat, V. Peres, L. Favergeon, *J. Nucl. Mater.* **2019**; *519*, 302.

[24] C. Duriez, M. Steinbrück, D. Ohai, T. Meleg, J. Birchley, T. Haste, *Nucl. Eng. Des.* **2009**; *239*, 244.

[25] C. Duriez, T. Dupont, B. Schmet, F. Enoch, *J. Nucl. Mater.* **2008***; 380*, 30.

[26] S. Guilbert-Bantia, A. Viretto, J. Desquines, C. Duriez, *J. Nucl. Mater.* **2021**; *548*. 152854.

[27] I .Idarraga, M . Mermoux, C. Duriez, A. Criscic, P. Mardon, *J. Nucl. Mater.* **2012**; *421*, 160.

[28] L. Zhang, M. J. Henson, S. S. Sekulic, *Anal. Chim. Acta*, **2005**; *545*, 262.

[29] R. Gautam, S. Vanga, F. Ariese, S. Umapathy, *EPJ Techn. Instrum.* **2015**; *2***,** 8.

[30] S. Piqueras, L. Duponchel, R. Tauler, A. deJuan, *Anal. Chim. Acta* **2011**; *705*, 182.

[31] J. E. Jackson, *J. Qual. Technol.* **2018**; *12*, 201.

[32] A. de Juan, J. Jaumot, R. A. Tauler, *Anal. Methods* **2014**; *6*, 4964.

[33] R. Guillou, M. Le Saux, E. Rouesne, D. Hamon, C. Toffolon-Masclet, D. Menut, J. C. Brachet, J. L. Béchade, and D. Thiaudière, *Mater. Charact.* **2019**; *158*, 109971.

[34] H. Swan, M. S. Blackmur, J. M. Hyde, A. Laferrere, S. R. Ortner, P. D. Styman, C. Staines, M. Gass, H. Hulme, A. Cole-Baker, P. Frankel, *J. Nucl. Mater.* **2016**; *479*, 559.

[35] M. Chollet, S. Valance, S. Abolhassani, G. Stein, D.l Grolimund, M. Martin, J. Bertsch, *J. Nucl. Mater.* **2017**; *488*, 181.

[36] E. Polatidis, P. Frankel, J. Wei, M. Klaus, R.J. Comstock, A. Ambard, S. Lyon, R.A. Cottis, M. Preuss, *J. Nucl. Mater.* **2013**; *432*, 102.

[37] B. Ensor, D. J. Spengler, J. R. Seidensticker, R. Bajaj, Z. H. Cai, A. T. Motta, *J. Nucl. Mater.* **2019**; 526, 151779.

[38] M. Sternik, K. Parlinski, *J. Chem. Phys*. **2005**; *122*, 064707.

[39] A. T. Motta, M. Gomes da Silva, A. Yilmazbayhan, R. Comstock, Z. Cai, and B. Lai, *Microstructural Characterization of Oxides Formed on Model Zr Alloys Using Synchrotron Radiation*, *Journal of ASTM International* 5, no. 3, pp. 1-20, **2008**.

[40] P. Barbéris, G. Corolleur-Thomas, R. Guinebretière, T. Merle-Mejean, A. Mirgorodsky, P. Quintard, *J. Nucl. Mater.* **2001**; *288*, 241.

[41] W. Spengler, R. Kaiser, *Solid State Commun.* **1976**; *18*, 881.

[42] X. Zhao, D. Vanderbilt, *Phys. Rev. B* **2002**; *65*, 075105.

[43] A. Kuwabara, T. Tohei, T. Yamamoto, I. Tanaka, *Phys. Rev. B* **2005**; *71*, 064301.

[44] C. W. Li, H. L. Smith, T. Lan, J. L. Niedziela, J. A. Muñoz, J. B. Keith, L. Mauger, D. L. Abernathy, B. Fultz, *Phys. Rev. B* **2015**; *91*, 144302.

[45] M. Cardona, M. L. W. Thewalt, *Rev. Mod. Phys.* **2005**; 77, 1173.

[46] C. Ciszak, M. Mermoux, G. Gutierrez, F. Leprêtre, C. Duriez, I. Popa, L. Fayette, S. Chevalier, *J. Raman Spectrosc*. **2019**; *50*, 425.

[47] A. Dieguez, A. Romano-Rodrıguez, A. Vila, J. R. Morante, *J. Appl. Phys.* **2001**; *90*, 1550.

[48] H. Buscail, R. Rolland, C. Issartel, S. Perrier, L. Latu-Romain, Corros. Sci. **2018**; *134*, 38.

[49] A. M. Huntz, *Mater. Sci. Technol.* **1988**; *4*, 1079.

[50] M. Guérain, C. Duriez, J.L. Grosseau-Poussard, M. Mermoux, *Corros. Sci.* **2015**; *95*, 11.

[51] I. De Wolf, *Semicond. Sci. Technol*. **1996**; 11, 139.

[52] J. F. Nye, *Physical Properties of crystals: their representation by tensors and matrices,* Clarendon Press, Oxford, **1957**.

[53] S. K. Chan, Y. Fang, M. Grimsditch, Z. Li, Z., M. V. Nevitt, W. M. Robertson, E. S. Zouboulis, *J. Am. Ceram. Soc.* **1991**; *74*, 1742.

[54] G. Fadda, L. Colombo, G. Zanzotto, *Phys. Rev. B* **2009**; *79*, 214102.

[55] X. S. Zhao, S. L. Shang, Z. K. Liu, J. Y. Shen, *J. Nucl. Mater.* **2011**; *415*, 13.

[56] N. Pétigny, P. Barberis, C. Lemaignan, Ch. Valot, M. Lallemant, *J. Nucl. Mater.* **2000**; 280, 318.

[57] P. Bouvier, *Etude Raman des distributions de phase et de contraintes dans des couches d'oxydation d'alliages de Zirconium,* PhD, Institut National Polytechnique de Grenoble, Grenoble, France, **2000**.

[58] G. Grimvall, *Thermophysical Properties of Materials*, North Holland, **1999**.

[59] R. J. Angel , M. Murri , B. Mihailova, M. Alvar, *Z. Kristallogr*. **2019**; *234*, 129.

[60] E. Anastassakis, A. Pinczuk, E. Burstein, F. H. Pollak, and M. Cardona, *Solid State Commun.* **1970**; *8*, 133.

[61] G. Pezzotti, *J. Appl. Phys.* **2013**; *113*, 211301.

[62] R. Korlacki, M. Stokey, A. Mock, S. Knight, A. Papamichail, V. Darakchieva, M. Schubert, *Phys. Rev. B* **2020**; *102*, 180101.

[63] Q. Ma, D. R. Clarke, *J. Am. Ceram. Soc.* **1993**; *76*, 1433.

[64] K. B. Chong, M. E. Fitzpatrick, *Surf. Coat. Technol.* **2017**; *324*, 140.

[65] L. Kurpaska, J. Favergeon, J-L. Grosseau-Poussard, L. Lahoche, G. Moulin, *Appl. Surf. Sci.* **2016**; 385, 106.

[66] M. Parise, O. Sicardy, G. Cailletaud, *J. Nucl. Mater.* **1998**; *256*, 35.

[67] D. J. Spengler, A. T. Motta, R. Bajaj, J. R. Seidensticker, Z. H. Cai, *J. Nucl. Mater.* **2015**; *464*, 107.

[68] H. L. Li, M.G. Glavicic, J.A. Szpunar, *Mater. Sci. Eng. A* **2004**; *366*, 164.

[69] V. Petukhov, High. Temp. High. Press. **2003/2004**; *35/36*, 15.

[70] G. A. Kourouklis, E. Liarokapis, *J. Am. Ceram. Soc*. **1991**; *74*, 520.

[71] G. Pezzotti, A. A. Porporati, *J. Biomed. Opt.* **2004**; *9*, 372.

[72] M. Ishigame, T. Sakurai, *J. Am. Ceram. Soc*. **1977**; *60*, 367.

[73] D. A. Daramola, M. Muthuvel, G. G. Botte, *J. Phys. Chem. B* **2010**; 114, 9323.

[74] N.S. McIntyre, M.J. Graham, *Study of Metal Corrosion and Oxidation Phenomenon Using Secondary Ion Mass Spectrometry,* in Analytical methods in corrosion science and engineering, P. Marcus, F. B. Mansfeld Ed., **2006**.

[75] S. N. Basu, J. W. Halloran, *Oxid. Met.* **1987**; *27*, 143.

[76] S. Chevalier, G. Strehl, J. Favergeon, F. Desserrey, S. Weber, O. Heintz, G. Borchardt, J. P. Larpin, *Mater. High Temp.* **2003**; *20*, 253.

[77] P. Fielitz, G. Borchardt, M. Schmücker, H. Schneider, Solid State Ion. **2003**; *60*, 75.

[78] M. Mermoux, C. Duriez, O. Coindreau, *Corros. Sci.* **2021** ; *184*, 109351.

[79] M. Guerain, M. Mermoux, C. Duriez, *Corros. Sci.* **2015** ; *98*, 140.

[80] B. K. Kim, H. O. Hamaguchi. *Phys. Stat. Sol. (b)* **1997**; *203*, 557.

[81] A. Kasperski, M. Guérain, M. Mermoux, F. Jomard, *Oxid. Met.* **2017***; 87*, 501.

[82] A. Kasperski, C. Duriez, and M. Mermoux, *Combined Raman Imaging and ^{18}O Tracer Analysis for the Study of Zircaloy-4 High-Temperature Oxidation in Spent Fuel Pool Accident*, in Zirconium in the Nuclear Industry: 18th International Symposium, R. Comstock and A. Motta Ed., West Conshohocken, PA: ASTM International, pp. 1059-1092, **2018**.

[83] Y. Mishin, C. Herzig, *Nanostruct. Mater.* **1995**; *6*, 859.